Accepted to Phys. Fluids 10.1063/5.0168351

Features and mechanisms of asymmetric wake evolution downstream of two parallel circular cylinders

Yuhao Yan[1†](严雨浩), Weilin Chen[1,2†](陈威霖), Zhimeng Zhang[1](张志猛), Chunning Ji[1*](及春宁), Narakorn Srinil[3]

[1]State Key Laboratory of Hydraulic Engineering Simulation and Safety, Tianjin University, Tianjin 300350, China.

[2]National University of Singapore, Department of Civil and Environmental Engineering, Singapore 117576, Republic of Singapore.

[3]School of Engineering, Newcastle University, NE1 7RU, Newcastle upon Tyne, United Kingdom.

Uniform flow past side-by-side circular cylinders is a classical fluid dynamic model that triggers rich phenomena, from which asymmetric wakes usually emerge. Such asymmetry arising from a completely symmetric geometric setting is of theoretical interest when exploring the system bifurcations. Using direct numerical simulation, a detailed parametric map of the wakes behind two side-by-side circular cylinders is first presented with several asymmetric wake patterns. These include asymmetric anti-phase (AAP), typical and special deflected (tDF and sDF), and in-phase (IP) flows, for which AAP and sDF flows are discovered for the first time. Additionally, the IP flow is simulated by both two- and three-dimensional grids to explore the effect brought by three-dimensional vortical structures. The evolution of these asymmetric wakes is analysed in different phases, with the aid of the wavelet transform, Hilbert-Huang transform, and dynamic mode decomposition, to reveal their temporal variations of developing features. Interestingly, although revealing with distinct fully-developed flow fields, there are several common dynamics identified among these wake patterns: AP and IP vortex shedding, wake transition, and gap flow oscillation. The vicissitudes of dynamic flow evolution allow us to further differentiate several wake patterns and ultimately contribute to a deeper understanding of asymmetric flows.

Key words: vortex dynamics, asymmetric flows, mode decomposition, side-by-side circular cylinders

1. Introduction

Owing to the complex flow interactions, the wakes downstream of a pair of side-by-side circular cylinders present several distinctive patterns. Understanding the physics of these wake patterns is tremendously important for engineering applications, such as the problem of flow over multiple undersea risers, heat exchange bundle tubes and pipelines, transmission lines, chimney stacks, and offshore

*Corresponding author: cnji@tju.edu.cn
†These two authors contributed to the paper equaly

floating platform columns (Zdravkovich, 1977; Sumner, 2010; Zhou and Alam, 2016, Muhammad at al. 2022, Mondal and Alam, 2023). This study numerically investigates the developments of asymmetric wake patterns behind two parallel circular cylinders and aims to advance the understanding of the wakes behind multiple circular cylinders.

Based on the previous studies, the wake patterns behind two circular cylinders in side-by-side arrangements can be classified into three different regimes as the spacing ratio (s/D, where s is the centre-to-centre distance of the two cylinders and D is the cylinder diameter) increases. These patterns include a single bluff-body (SB) flow, deflected (DF) flow, and coupled flow (Bearman and Wadcock, 1973; Sumner et al., 1999; Sumner, 2010; Zeng et al., 2023). At a small s/D ($\leq$ 1.1–1.2), the gap flow between the two cylinders is insignificant, and vortices are alternately shed from the freestream sides of the two cylinders (Wang et al., 2002; Afgan et al., 2011; Supradeepan and Roy, 2014). Thus, an extended bluff body with a diameter of $s + D$ embraced by the freestream-side shear layers of the cylinders appears. However, at a large s/D ($\geq$ 2.2–2.5), the vortices are freely shed from both sides of the two cylinders, and the coupling between the two cylinders becomes significant. Depending on s/D and Reynolds (Re) number, both in-phase (IP) and anti-phase (AP) flows can be observed, with the latter dominating at a larger s/D (Bearman and Wadcock, 1973; Williamson, 1985; Peschard and Le Gal, 1996; Sumner et al., 1999; Meneghini et al., 2001). Williamson (1985) investigated these two IP and AP flow patterns by the water tunnel experiments and found that the IP vortex street is perceived only in the near wake because of the pairing, splitting, and emergence of the co-rotating vortices. Contrastingly, they found that the AP vortex street is stable and can maintain its shape within a long downstream distance. Further, Williamson (1985) reported the coexistence of the IP and AP flows in special s/D cases.

At an intermediate s/D (1.1–1.2 < s/D < 2.2–2.5), the gap flow is developed significantly from the extended regime and it can be stably or alternatively biased toward the two cylinders, leading to the dominance of DF or flip-flopping (FF) flow, respectively (Bai et al., 2020; Ullah and Zhou, 2020). Correspondingly, the wake widths of the two cylinders are no longer identical (Bearman and Wadcock, 1973; Kim and Durbin, 1988; Alam et al., 2003; Afgan et al., 2011; Wu et al., 2020). For the cylinder with a narrow wake, the roll-up shear layer is closer to the cylinder's rear side; thus, compared to the other cylinder, the vortex shedding frequency and the drag force are larger (Roshko, 1954; Alam et al., 2003). For the FF flow, the switching time of the gap flow strongly depends on s/D and Re (Kim and Durbin, 1988; Kang et al., 2003; Brun et al., 2004). Kim and Durbin (1988) observed that, in a high-Re

turbulent flow, the switching time of the gap flow is several orders of magnitude longer than the vortex shedding period. As *Re* increases, the mean switching time between flip-flops decreases gradually. However, in a laminar flow, the switching time is contrastingly shorter, which is only several times the vortex shedding period (Kang, 2003; Carini et al., 2014, 2015).

Several wake patterns behind two parallel circular cylinders have been described through numerical simulations in a wide parametric space with small increments. Kang (2003) numerically investigated the wakes of a pair of side-by-side circular cylinders at *Re* = 40–160 and *s*/*D* = 1.0–6.0. In their study, six different flow patterns, i.e., AP, IP, FF, DF, SB, and steady state (SS) flows, were revealed. The significant dependence of each pattern on *Re* and *s*/*D* was also highlighted. Moreover, the author identified some bifurcations that existed between DF and FF flows and between IP and AP flows, owing to initial condition changes. Similar phenomena were also reported by Xu et al. (2003), Singha et al. (2016), Ren et al. (2021), and Qi et al. (2023). By considering *Re* at lower values, Liu et al. (2007) classified the wakes behind two side-by-side circular cylinders into nine patterns, including four steady flow patterns (SB flow, separated double-body steady flow, biased steady flow, and transition steady flow) and five unsteady flow patterns (single bluff-body periodic, biased quasi-steady, FF, IP, and AP flows). By considering higher *s*/*D* values, Supradeepan and Roy (2014) studied the wakes of two side-by-side circular cylinders at a constant *Re* (= 100) and reported five wake patterns including the single bluff-body periodic flow (*s*/*D* = 1.1–1.3), aperiodic flow (same to the FF flow reported in other studies, *s*/*D* = 1.4–2.2), transition flow (*s*/*D* = 2.3–3.1), AP flow (*s*/*D* = 3.2–7.9), and IP flow (*s*/*D* ≥ 8.0), as *s*/*D* is consecutively increased. Singha et al. (2016) numerically studied the wakes of two parallel circular cylinders at *Re* = 20–160 and *s*/*D* = 1.2–5.0. In all cases, five unsteady wake patterns, i.e., SB, DF, FF, IP, and AP flows, were documented. Using a two-dimensional simulation, Pang et al. (2016) investigated the wakes of two side-by-side circular cylinders at *Re* = 6.0×10^4 and *s*/*D* = 1.1–7.0, and reported five different wake patterns, i.e., SB flow at *s*/*D* = 1.1–1.2, asymmetric flow at 1.2 < *s*/*D* ≤ 2.6, and three coupled flows (IP, AP, and hybrid (HB) flows) at 2.6 < *s*/*D* ≤ 7.0. A similar investigation was conducted by Shao and Zhang (2008) where both biased and coupled patterns were revealed.

At high *Re*, 3-D wakes of two parallel circular cylinders were examined by direct or large-eddy numerical simulations. Afgan et al. (2011) studied the wakes of two side-by-side circular cylinders at *Re* = 3×10^3 and *s*/*D* = 1.0–5.0 by using large eddy simulations. At the intermediate *s*/*D* (= 1.25–1.75), the gap flow randomly switches its direction, with multiple frequencies detected in the near wake. At the large s/D (≥ 2.0), the vortices shed from the two cylinders are anti-phased, thus forming a symmetrical wake. Tong et al. (2015) considered $Re = 10^3$ and found that a strong three-dimensionality exists in the gap between two side-by-side circular cylinders and this significantly affects the vortex interactions. Thapa et al. (2015) examined the wakes of two side-by-side circular cylinders at $Re = 500$ and $s/D = 1.5$–6.0 by using direct numerical simulations and observed DF and FF flows at $s/D = 1.5$ and 2.0, respectively. At $s/D = 4.0$ and 6.0, the interferences of the two cylinders become weak such that the AP flow appears. With a finer increment of s/D, Chen et al. (2022) identified five different wake patterns, i.e., SB flow at $s/D = 1.1$, DF flow at $s/D = 1.2$–1.8, FF flow at $s/D = 2.0$–2.4, HB flow at $s/D = 2.5$, and AP flow at $s/D = 2.7$–5.0 for $Re = 500$. Additionally, they found that 3-D vortical structures significantly weaken the vortex interactions by absorbing energy from the spanwise vortices and a longer cylinder could result in the growing switching time of the gap flow in the FF wake.

Several experiments have been carried out to reveal the intrinsic features of the wakes of two parallel circular cylinders in a strong turbulent flow, in comparison with those in the laminar flow. Three wake patterns, namely SB flow at the small s/D (< 1.1–1.2), synchronized (IP, AP, and HB) flow at the large s/D (> 1.75–2.0), and biased gap flow at the intermediate s/D, were reported (Sumner et al., 1999; Zhou et al., 2002; Alam et al., 2003; Wang and Zhou, 2005). The borders (s/D values) of different patterns in the turbulent flow are slightly smaller than those in the laminar flow because of the decreased viscous effect. That is, the wake transition from one to another occurs earlier as a result of increasing Re. Alam and Zhou (2007) experimentally studied the weak gap flow between two side-by-side circular cylinders at $Re = 6.0\times10^4$ and found that at $s/D = 1.1$, the gap flow is highly biased, thus giving rise to a separation bubble at the base of one cylinder. At $s/D = 1.2$, the separation bubble was not observed. The authors noticed two types of discontinuous changes in the flow structures at $s/D = 1.13$: one is due to the gap flow switching from one side to the other, and the other is due to a burst of the separation bubble.

From the above review, the wakes downstream of two parallel cylinders have been investigated extensively; however, the wake developments and modal contributions have not been fully understood. In this study, we aim to investigate the evolution of the asymmetric wakes downstream of the parallel cylinders by using modal analysis and uncover their intrinsic features and mechanisms. The rest of this paper is structured as follows. In Section 2, details of the adopted numerical methodology and modal analysis method based on the dynamic mode decomposition (DMD) are presented. In Section 3, we present the wake map of two side-by-side circular cylinders and then discuss modal analyses of the asymmetric wakes in different phases. The main findings of this paper are summarized in Section 4.

2. Numerical methodology and validation

2.1 Numerical methodology

The governing equations of the fluid flow and the cylinder wake are the incompressible Navier–Stokes equations, defined as follows.

$$\frac{\partial \boldsymbol{u}}{\partial t} + (\boldsymbol{u} \cdot \nabla)\boldsymbol{u} = -\frac{1}{\rho}\nabla p + \nu \nabla^2 \boldsymbol{u} \quad (2.1)$$

$$\nabla \cdot \boldsymbol{u} = 0 \quad (2.2)$$

where $\boldsymbol{u}$ is the velocity, p is the pressure, ∇ denotes the gradient operator, and ν is the kinematic viscosity. Direct numerical simulations of the uniform flow over two side-by-side circular cylinders are performed with the DMD data collections, using Nektar++ with a fourth-order accuracy. Specifically, Equations (2.1, 2.2) are numerically solved by applying the open-source framework Nektar++ (Cantwell et al., 2015; Xu et al., 2018; Moxey et al., 2020) using the spectral/hp element method (Karniadakis and Sherwin, 2005). The fourth-order polynomials are adopted for achieving improved numerical stability. A high-order splitting scheme (Karniadakis et al., 1991) is employed for the time integration by using an approach proposed by Guermond and Shen (2003), see www.nektar.info for greater details.

As shown in Fig. 1, the computational domain is set as [-25D, 20D] × [-25D, 25D] in x and y directions, respectively, with the origin located at the middle point between the two cylinders. The inflow boundary with the Dirichlet boundary conditions ($u = U_\infty$; $v = 0$) is 25D upstream of the center of the cylinders, while the outflow boundary with the Neumann boundary conditions ($\partial u/\partial x = \partial v/\partial x = 0$) is 20$D$ downstream. The top and bottom boundaries are set as free-slip boundaries ($\partial u/\partial y = 0$; $v = 0$). The cylinder surfaces are treated as no-slip boundaries with $u = v = 0$. For the pressure, $p = 0$ is set at the outflow boundary while $\partial p/\partial n = 0$ is set at other boundaries.

A structured mesh is generated by applying the finite element mesh generator Gmsh. To guarantee the accuracy of the simulations, the mesh is refined in the x-y plane near the cylinders in a region of 2D in the x direction and 4D in the y direction, with the smallest grid size near the cylinder of about D/64. Before a tenable simulation is conducted, validations should be made in comparison with previous literature (Kang 2003). Such validations include both mesh size and time step ($\Delta t U_\infty/D$) to balance accuracy and efficiency. Figure 2 presents brief validation and convergence tests for mesh size and time step. Meshes I to III are based on the 2-D meshing, Mesh II* (shown in 3.4.2) is a 3-D meshing that is extended from Mesh II (i.e., Meshes II and II* have the same x-y plane projection). Meshes II and II* are applied in the following 2-D and 3-D simulations with time step $\Delta t U_\infty/D = 0.01$, respectively.

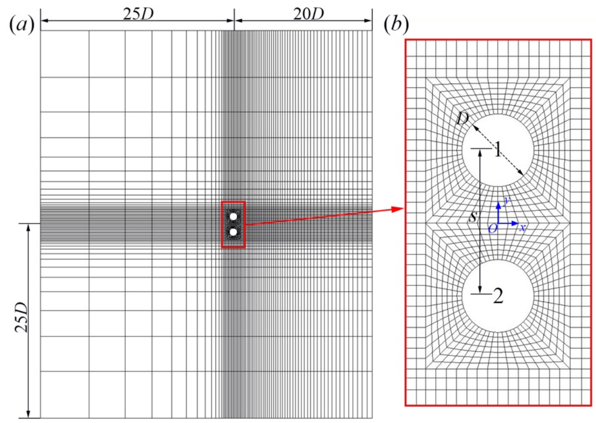

FIG. 1. Computational mesh: (*a*) *x-y* plane, (*b*) close-up view.

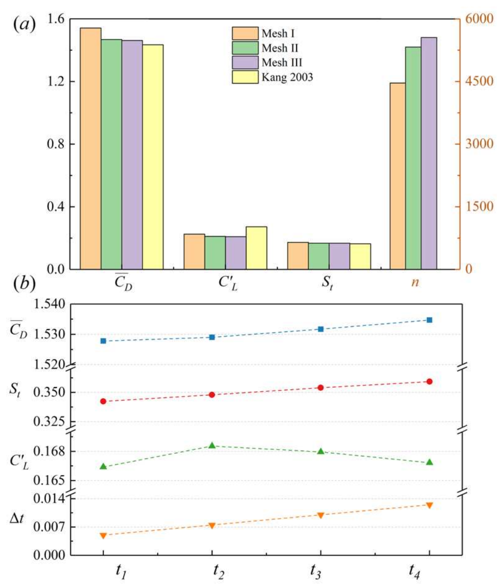

FIG. 2. Validation and convergence tests of Nektar++ simulations for uniform flow past two parallel circular cylinders at *Re* = 100 and *s*/*D* = 2.5: (*a*) mesh size of Meshes I to III (*n* is the number of quadrangles), and (*b*) time step validation of Mesh II at $t_1 = 0.005$, $t_2 = 0.0075$, $t_3 = 0.01$, and $t_4 = 0.0125$).

2.2 Dynamic mode decomposition (DMD)

As a data-driven and equation-free data analysis method pioneered by Rowley et al. (2009) and Schmid (2010), DMD is commonly used in several academic fields for its availability to identify eigenmodes of a high-dimensional system based purely on data from a simulation or experiment. In this paper, we follow the same procedure of Kutz et al. (2016), which is a Single Value Decomposition (SVD)-based structure that allows a low-dimensional truncation. The main idea of this method is the linear dynamic system assumption: X = AX', where X is a data matrix with columns being the first n-1 snapshots, and X' contains the last n-1 snapshots. Using SVD of X, one can derive the eigen-decomposition of the constant matrix A, which gives important dynamics of the flow evolution, during the observation where n snapshots are taken. Eigenvectors ϕ_i ($i = 1, \ldots, n$) present the spatial distribution, and the eigenvalues provide the growth rate (real part μ_r) and frequency component (imaginary part μ_i), while their amplitude variations can further help to characterize the temporal dynamics of each eigenmode. These factors contribute to the identification of dominant and important DMD modes.

Our goal here is to employ this DMD method to decompose the non-linear and high-dimensional system of flow around two side-by-side cylinders, to distinguish eigenmodes representing different dynamics in the flow evolution, and to further understand the flow itself. From this point of view, we investigate typical flow pattern cases of this system, separate the flow development into several periods, and perform DMD analysis on each period to see if certain DMD modes change in successive phases within a transient evolution. We recognize the dynamics through a combination of spatial distribution, growth rate, frequency, and temporal variations. Thus, DMD modes with similar spatial distributions and frequencies are represented by the one with the largest initial amplitude, and the temporal dynamics are presented by the initial amplitude at the beginning of each period, for simplicity. As later shown in Section 3, some DMD modes possess a trivial amplitude at the beginning but yet play an important role in the following flow development. Therefore, we avoid using methods such as the Sparsity-promoting DMD (SP-DMD, Jovanovic et al., 2014) that may occasionally filter out some DMD modes. For a similar reason, the Recursive DMD (R-DMD, Noack et al., 2016) that is known to have a stronger ability to handle the transient fluid dynamics is not considered here, as the orthogonality and well-defined amplitude variation are not required here.

For a typical flow pattern, we separate the flow evolution into five phases based on their development characteristics. In each phase, we collect snapshots with a time interval at $\Delta t U_\infty / D = 0.5$

and then perform the DMD to examine each modal variation, to identify the dynamics represented by certain modes, using spatial distributions ϕ_i (I = 1, …, n), eigenvalue components μ_r and μ_i, frequencies f_{DMD} = Im(ln(μ_r+iμ_i)/2πΔt), and initial amplitudes b_i^*. To ensure comparability, DMD amplitudes shown here are normalized, i.e., b^* values are amplitude proportions represented by each mode for each DMD analysis.

3. Results and discussion

To explore how the wake asymmetry develops from a symmetric geometric setting, we first introduce the overall distribution of different wake patterns on the parametric space and then perform the detailed modal analysis on asymmetric wake patterns using the flow visualization, wavelet transform (WT), Hilbert-Huang transform (HHT), and DMD analyses.

3.1 Summary of wakes behind two side-by-side circular cylinders

Figure 3 shows the wake patterns of two side-by-side circular cylinders at Re = 50–175 and s/D = 1.0–5.0, which can be considered as a refinement of the classic one introduced by Kang (2003). As shown in Fig. 3, seven different patterns are recognized in the examined parametric space, namely steady state (SS) flow, single bluff-body (SB) flow, deflected (DF) flow, in-phase (IP) flow, anti-phase (AP) flow, flip-flopping (FF) flow, and asymmetric anti-phase (AAP) flow. The vorticity contours for these flow patterns are displayed in Fig. 4.

As shown in Fig. 4(a), the SS flow field behind the two cylinders is stable, persisting to appear at a slightly higher Re than the critical Re (≈ 47) for a single circular cylinder (Giannetti and Luchini, 2007; Marquet et al., 2008; Jiang et al., 2016; Park and Yang, 2016). The SB flow occurs at a small s/D. Demarcated by Re = 95, the SB flow dominates over a wider region with decreasing Re while it remains approximately constant for Re > 95. Because of the small s/D, the gap flow between the two cylinders is weak, and the gap-side shear layers show no distinct oscillations (Fig. 4(b)). Therefore, vortices are only shed from the freestream sides of the two cylinders, leading to the two cylinders being like an extended bluff body (Zhou et al., 2001; Kang, 2003; Xu et al., 2003; Wang and Zhou, 2005). For the DF flow, the gap flow persistently biases toward one cylinder (Fig. 4(c)). Compared to the SB flow, the DF flow occurs at a larger s/D and the region width depends strongly on s/D and Re. The green-hatched region in Fig. 3 denotes a bistable flow regime in which either the DF or FF2 flow appears depending on the initial conditions. However, the DF flow in this region is slightly different from the typical DF (tDF) flow reported by Kang (2003), Liu et al. (2007), and Chen et al. (2020), as the deflected gap flow shows a perceivable oscillation, which is not observed in the tDF flow. It is thus named the special DF (sDF) flow. As shown later, a low frequency is detected from the signals of unsteady drag and lift forces, which are associated with the sway of the gap-side shear layers.

The FF flow is detected at a larger s/D than the DF flow, which is in line with the requirement of a stronger gap flow to switch its direction, see Fig. 4(*d*,*e*) (Chen et al., 2020). According to the origin, the FF flow is further divided into two patterns (FF1 and FF2) stemming from the IP and AP synchronized vortex shedding instabilities, respectively (Chen et al., 2023). Further increasing s/D, IP and AP flows dominate successively (Williamson, 1985; Kang, 2003). For these two patterns, the vortices from the same side of the two cylinders are in AP and IP behaviours, respectively (Fig. 4(*f*,*g*)). There is another IP flow region observed below the FF1 flow and its corresponding s/D is comparable to that of the FF flow. To differentiate the two IP regions, the smaller one below the FF1 flow is named IP_1 while the larger one is IP_2. As displayed in Fig. 3, the width of IP_2 flow diminishes quickly with increasing s/D after $Re > 75$, which suggests that the IP flow may not be able to exist in the high-*Re* turbulent flow (Kang, 2003; Chen et al., 2022), as will be discussed later. The AP flow dominates over a wider region than other flows. As *Re* increases, the width of AP flow augments gradually (Williamson, 1985; Sumner et al., 1999; Kang et al., 2003; Xu et al., 2003). Owing to the large s/D, vortices of the two cylinders exhibit weak interactions and the vortex street can thus maintain its alignment in a longer downstream distance (Williamson, 1985). The AAP flow is observed at Re ≈ 50 and $s/D \approx 2.4$–4.5 for which vortices from the two cylinders are anti-phased. Because the shear layer fluctuation of one cylinder is stronger than the other cylinder, the wake becomes asymmetric with respect to the incoming flow (Fig. 4(*h*)).

To sum up, in the laminar flow, several asymmetric wakes, i.e., SB, DF, FF, AAP, and IP flows, are identified. To look deep into the flow developments of these patterns and discuss how the asymmetry arises from a symmetric condition, we provide comprehensive modal analyses of DF, AAP, and IP flows in the following sections. However, it is worth pointing out that because the development of SB flow is similar to the vortex shedding of a single circular cylinder and the development of FF flow has been discussed in great detail in Chen et al. (2023), SB and FF flows will not be investigated in this study.

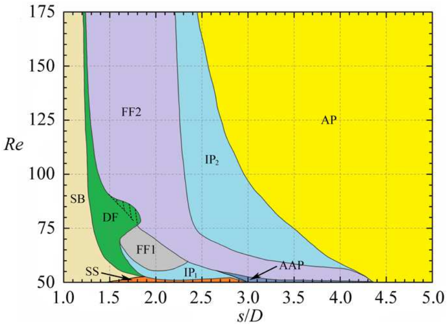

FIG. 3. The wake behind two side-by-side circular cylinders at *Re* = 50–175 and *s*/*D* = 1.0–5.0, adapted from Chen et al. (2023). The borders of different patterns are determined by the simulations beginning from the rest. Depending on the initial condition, the green-hatched region can be DF or FF2 flow.

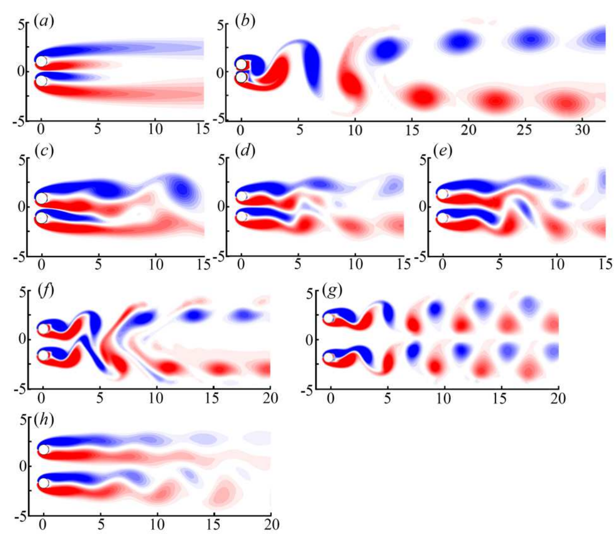

FIG. 4. Vorticity contours for the flow patterns in Fig. 3: (*a*) SB at *s*/*D* = 1.2 and *Re* = 100, (*b*) DF at *s*/*D* = 1.7 and *Re* = 80, (*c*) AAP at *s*/*D* = 3.3 and *Re* = 50, (*d*) IP at *s*/*D* = 2.5 and *Re* = 120, (*e*) AP at *s*/*D* = 4.0 and *Re* = 100, (*f*) SS at *s*/*D* = 1.8 and *Re* = 50, (*g*) FF1 at *s*/*D* = 2.0 and *Re* = 60, and (*h*) FF2 at *s*/*D* = 2.3 and *Re* = 64.

3.2 Evolution of asymmetric anti-phase flow

The asymmetric anti-phase (AAP) flow has a great similarity to the symmetric and stable anti-phase (AP) flow, with a biased yet periodic flow field. This is suitable as an introduction to how the asymmetry grows from a symmetric setting. Based on the temporal characteristics of drag and lift coefficients, the development of the flow is divided into five different phases, namely Phase I to V. In general, the flow stays symmetric, with the two cylinders drag force curves overlapping in Phase I. In Phase II, these two curves begin to bifurcate and show asymmetry; such a departure becomes noticeable in Phase III. In Phase IV, the alteration of two vortex streets slows down but it is still unstable. In Phase V, the flow is fully developed with a stable vortex shedding. As such, the flow development from Phase I to V covers the emergence, transition, and dissipation of instability, from which the flow asymmetry appears. To further illustrate the flow-developing features over these five phases, we conduct the WT analysis of drag and lift coefficients, showing the temporal variations of the dominant frequencies. Here, the complex Morelet function is adopted (Alam et al., 2003; Zhao et al., 2012; Chen et al., 2015, 2020) and the non-dimensional frequency is set as 6 to avoid using the correction terms (Farge, 1992). Moreover, to establish deeper connections between the frequency variation and the flow field change, we perform DMD analysis in each phase by collecting *z*-vorticity snapshots with a time interval of $\Delta t U_\infty / D = 0.5$. Combining the spatial distribution, frequency character, and amplitude variation of DMD modes in each phase, we illustrate the evolution process of the AAP flow at $s/D = 2.3$ and $Re = 50$.

As the flow past through the gap region is restricted by the geometric distribution of the two cylinders, the shear stresses on the surface of the upper and lower cylinders and the vortex rotation directions are perfectly opposite to each other. This is the main reason why the AP vortex shedding is always expected to take place at the beginning of almost all of the flow patterns (Mizushima and Ino, 2008). As seen from Fig. 5(*a*,*b*), in Phase I ($t^* < 1300$), the vortex shedding manifests a typical AP manner, characterized by the overlapped drag coefficients and the AP lift coefficients of the two cylinders. As shown in Fig. 5(c_1,d_1,e_1), in this phase, the vortex shedding is periodic, with a dominant frequency at $f = 0.14$. Vortices are shed from the two cylinders at $x/D \approx 5.0$, with the vortex street being perfectly symmetric to the incoming flow regardless of the vortex rotations. As shown in Fig. 6(*a*–*c*), the corresponding DMD mode with the AP vortex street and initial amplitude at $b^* = 41\%$ (this value is normalized over this phase to ensure comparability) and its second harmonic (not shown here) dominate this phase. Interestingly, another mode at the same frequency but with an IP vorticity distribution can also be found in this phase, although with only a trivial initial amplitude ($b^* < 1\%$). In Phase II ($t^* = 1300$–1500), the discrepancy of drag coefficients of the two cylinders gradually becomes noticeable, but the two modes that have a clear relation with the vortex shedding are very similar to those in Phase I. In addition, a mode with $f = 0$ that is slightly outside of the limit circle is observed in the first two phases, see Fig. 6(*a*,*e*). We suppose such a mode acts like a shift mode that was first introduced by Noack et al. (2003). The shift mode quantifies the distortion between the base flow and the mean flow, caused by the Reynolds stress (Barkley, 2006; Turton et al., 2015; Deng et al., 2020). In other words, this mode might not be intuitive, but it indicates a transition states of the flow and signifies how much the system changes from its previous equilibrium. Thus, this mode might play a role in triggering a further wake transition.

In Phase III ($t^* = 1500$–1720), as the drag coefficients of the two cylinders bifurcate, the wake becomes asymmetric, see Fig. 5(a,e_3). On the one hand, the asymmetry is featured by the smaller wake width and the larger vortex formation/shedding length of the upper cylinder. Correspondingly, the upper cylinder has a smaller mean drag and lift amplitude than that of the lower cylinder, as shown in Fig. 5(*a*,*b*). Due to the narrow-wide and long-short vortex shedding, the dominating vortex shedding mode at $f = 0.14$ is asymmetric with a higher z-vorticity in the wake of the lower cylinder, but the spatial distribution of the two vortex streets is AP in general. Meanwhile, there is a slightly out-of-phase mode at $f = 0.13$ with the lower cylinder's wake showing a stronger vorticity, which may evolve from the IP mode at $f = 0.14$ in the first two phases, as they have rather similar spatial distributions. If this connection were to be established, then one could expect that the initial amplitude discrepancy between the two vortex shedding modes ($b^* = 25\%$ and 5% for the AP-like and IP-like mode, respectively) narrows in this phase than before. On the other hand, different from other asymmetric (e.g., DF and FF) patterns, the gap flow in the AAP pattern is parallel to the incoming flow, with no perceivable fluctuations observed. The non-fluctuating gap flow can be further proved by the DMD mode at $f = 0.01$ (the only mode near $f = 0$, see Fig. 6(*i*)) where there is no significant z-vorticity concentrating within the gap flow region (see Fig. 6(*l*)). Noticeably, the z-vorticity strength of this mode appears in the wake region downstream of the cylinders, which may suggest the interactions between the AP-like mode at $f = 0.14$ (see Fig. 6(*j*)) and the IP-like mode at $f = 0.13$ (see Fig. 6(*k*)). Based on the above discussions, we argue that the wake dynamics in the AAP flow are different from those in other DF and FF flows where the pitchfork bifurcation (Carini et al., 2014; Liu and Jaiman, 2016; Yan et al., 2020, 2021) shapes the wake pattern. This will be discussed in the next section.

Afterwards, in Phase IV ($t^* = 1720$–2050) and V ($t^* > 2050$), the wake asymmetry becomes more apparent. As shown in Fig. 5(e_4,e_5), the shear layers of the lower cylinder exhibit stronger fluctuations than those of the upper cylinder. Thus, vortices with higher strengths appear in the lower-cylinder wake.

This agrees well with the higher mean drag and fluctuating lift coefficients, as shown in Fig. 5(*a*,*b*). However, as indicated by the zoom-in views in Fig. 5(*a*,*b*), the force coefficients of the two cylinders are not perfectly synchronized. We, therefore, conduct a separate phase analysis of these curves towards $t^* =$ 2050–3000 through the HHT (Huang et al., 2009, 2014) following the same procedure as in Liu and Jaiman (2016), see Fig. 7. The HHT results confirm that the phase lag between the lift coefficients of the two cylinders slightly fluctuates at about 0.94π (≈ 169.7°), which verifies that the two vortex streets are not strictly anti-phased, and the fluctuation also indicates a small frequency difference. Even though the WT result seems failed at capturing such a difference because of the frequency resolution, the sole dominant frequency is recognized as $f = 0.14$ in Fig. 5(c_4,c_5). Correspondingly, the DMD mode of the vortex shedding at this frequency dominates these two phases ($b^* > 13\%$). Because of the symmetry breaking in the wake, such the vortex shedding mode with vaguely AP vortex streets has higher *z*-vorticity concentrating in the lower vortex street, see Fig. 6(*n*,*r*). Meanwhile, although with a smaller initial amplitude, another vortex shedding mode at $f = 0.13$ with a stronger *z*-vorticity in the upper vortex street, is also detected by the DMD analysis, see Fig. 6(*o*,*s*). Noticeably, the initial amplitude of this $f = 0.13$ mode decreases from $b^* = 3.7\%$ in Phase IV to $b^* = 0.4\%$ in Phase V, which quantifies the process of the $f = 0.14$ mode taking the sole dominance, see Fig. 6(*m*,*q*).

Compared to the classical AP flow with two perfectly AP vortex streets, the AAP flow is featured by the narrow-wide and long-short vortex shedding while the two asymmetric, yet independent, vortex streets are kept anti-phased in general. As for the wake development, the flow starts with a symmetric AP vortex shedding, although two vortex shedding modes appear in the DMD spectrum: an AP one with a dominant initial amplitude, and an IP one with only a trivial amplitude. In the next phases, when the asymmetry of the wake emerges and the force coefficients begin to bifurcate, the amplitude of this IP mode increases. During the wake transition, a shift mode that measures the base flow alteration, as well as a mode that matches the slow fluctuating gap flow, are also detected. Eventually, the two vortex streets become stable at the phase lag of 169.7°, suggesting the vortex shedding is not strictly anti-phased. Correspondingly, the IP mode disappears and the two modes with opposite strength on each side predominate the wake, which are loosely AP distributed. This means that the AAP flow is not determined by a single dynamics, which is different from the AP flow. The development of asymmetry usually grows with DMD modes that have a clear connection to the wake region in terms of the spatial distribution.

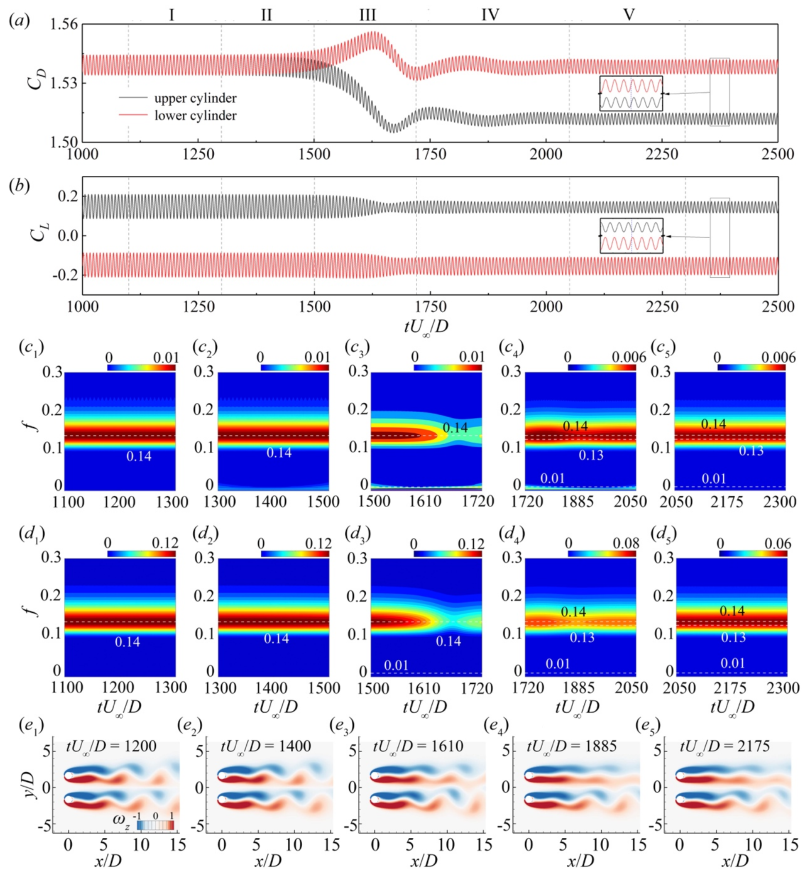

FIG. 5. Evolution of the AAP flow at s/D = 3.3 and Re = 50: (a,b) time histories of the drag and lift coefficients, (c,d) WT results of the drag and lift coefficients of the upper cylinder, and (e) vorticity contours. (c_1,d_1,e_1) for the initial phase at t^* = 1100–1300, (c_2,d_2,e_2) for the developing phase at t^* = 1300–1500, (c_3,d_3,e_3) for the transient phase at t^* = 1500–1720, (c_4,d_4,e_4) for the pre-stable phase at t^* = 1720–2050, and (c_5,d_5,e_5) for the stable phase at t^* = 2050–2300. Here, I, II, III, IV, and V in (a) and (b) denote the initial, developing, transient, pre-stable, and stable phases, respectively.

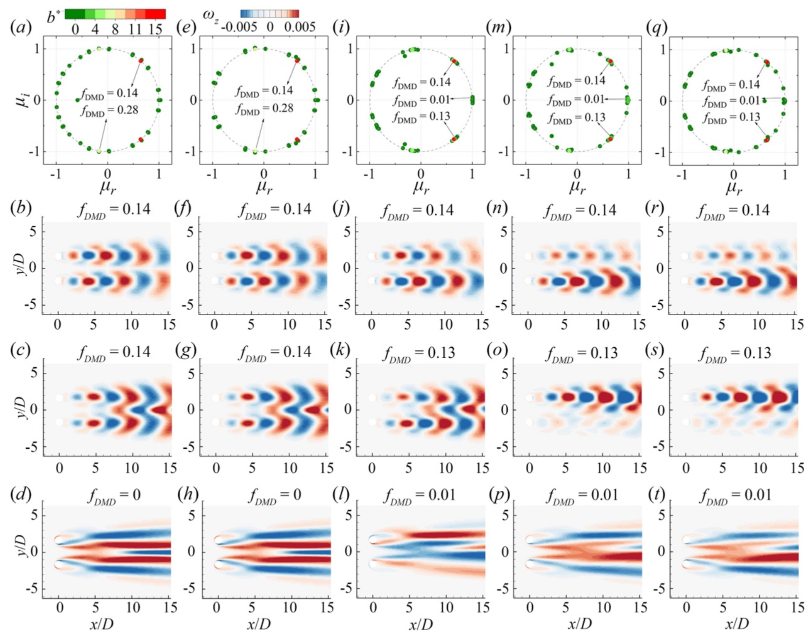

FIG. 6. DMD spectrum and modes with the most significant amplitude b^* at s/D = 3.3 and Re = 50: (*a*–*d*) for the initial phase at t^* = 1100–1300, (*e*–*h*) for the developing phase at t^* = 1300–1500, (*i*–*l*) for the transient phase at t^* = 1500–1720, (*m*–*p*) for the pre-stable phase at t^* = 1720–2050, and (*q*–*t*) for the stable phase at t^* = 2050–2300.

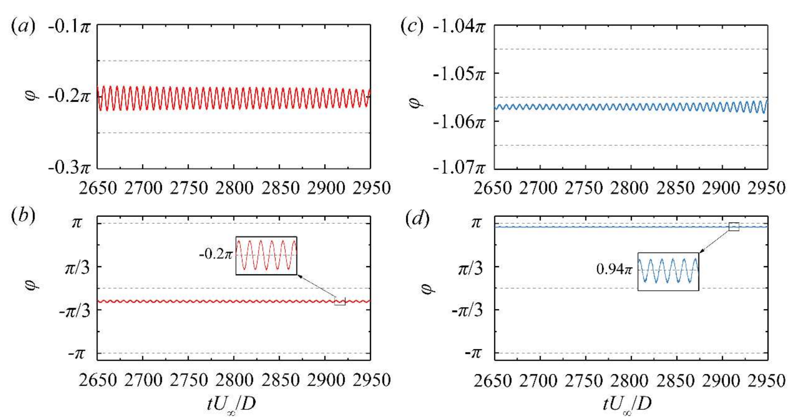

FIG. 7. Phase lag of the force coefficients between the upper and lower cylinders, calculated by HHT. (*a*,*b*) for the drag coefficients and (*c*,*d*) for the lift coefficients.

3.3 Evolution of deflected flow

The deflected (DF) flow is featured by a biased gap flow and asymmetric vortex shedding. According to the summary in Section 3.1, two types of DF flow have been shown here: typical DF and special DF. We select two cases to display the characteristics of these two DF flows. Following the similar routine in Section 3.2, the flow developments of these flows are divided into five phases based on temporal features of the forces for which each phase is analysed using WT, HHT, and DMD methods with the same parameters.

3.3.1 Evolution of typical deflected flow

Following the temporal variation of flow features and corresponding frequency characters, we first focus on the typical DF (tDF) flow by analyzing the case at s/D = 1.7 and Re = 80. As shown in Fig. 8(a,b,e_1), in Phase I (t^* < 313), the flow around the two cylinders remains approximately stable in the near wake region, with slightly fluctuating drag and lift coefficients. These mainly result from the weakly swinging shear layers in the far wake, which is in agreement with previous observations that the instability in the cylinder wake first appears in the far wake (Zdravkovich, 1997; Heil et al., 2017). WT results in Fig. 8(c_1,d_1) suggest that the dominant frequency in the lift force is at f = 0.12, while that in the drag force is much lower, i.e. f = 0.01. The DMD mode shown in Fig. 9(b) shows the vortex shedding frequency at f = 0.12 which has a dominant initial amplitude b^* = 47%. Noticeably, its spatial distribution of vorticity suggests that the vortex streets behind the two cylinders are in an AP behaviour and their strengths are higher at a farther downstream distance. On the contrary, the low-frequency mode that matches the dominant frequency (f = 0.01) of the drag force has a rather small initial amplitude b^* < 2%. As shown in Fig. 9(d), most z-vorticity of this mode concentrates within the gap region of the two cylinders ($x^* \lesssim 5$), which indicates the association with the gap flow. In addition, there is another DMD mode that has a spatial distribution likely related to the vortex shedding, as shown in Fig. 9(c), with a slightly lower frequency f = 0.10 and a trivial initial amplitude b^* < 1%. The vortex streets of such a mode are in an IP behaviour for which the high z-vorticity concentrates on the more upstream region ($x^* \approx 5$) and decays gradually downstream. It should be mentioned that the flow is highly transient and unstable at the initial phase. As a result, most modes fall out of the unit circle in Fig. 9(a), and a symmetric DMD mode with a real eigenvalue at f = 0 is also shown in Fig. 9(e).

In Phase II (t^* = 313–437), as indicated by the time histories of the force coefficients in Fig. 8(a,b), an IP vortex shedding arises significantly from $t^* \approx 350$. After that, it can also be noticed from Fig.

8(c_2,d_2) that the vortex shedding frequency gradually grows, which is associated with the change in the vortex dynamics induced by the continuous feedback of unstable vortex interactions in the far wake (Ho and Huerre, 1984; Huerre and Monkewitz, 1990). Correspondingly, DMD results in Fig. 9(*g*,*h*) suggest that two modes describe the vortex shedding behaviours with comparable initial amplitude ($b^* \sim 4\%$) and IP vortex streets, which is in line with the instantaneous IP vorticity contour shown in Fig. 8(e_2). The DMD mode at $f = 0.13$ can be attributed to the wake dynamics in the second half phase while the DMD mode at $f = 0.10$ might be a result of the wake dynamics in the first half phase. Comparing these modes with those in Phase I, a few differences can be remarked: i) due to a clear IP vortex shedding, all related modes are in an IP behaviour; ii) vortices are shed from the two cylinders at a much closer location to the cylinder base, as shown in Fig. 8(e_2). In other words, unlike Phase I, the vortex shedding modes in Phase II are more concentrated on the near wake. In addition, owing to the evident transient behaviour, the drag coefficient in the developing phase is also dominant by a DMD mode ($f = 0.004$, $b^* = 30\%$) that acts like a shift mode in Noack et al. (2003), representing the slowly changing base flow.

In the subsequent phases ($t^* > 437$), the asymmetry of the flow field develops. As shown in Fig. 8(*a*,*b*), in Phase III ($t^* = 437$–550), the envelopes of drag and lift coefficients become FF-like, featured by an intermittent switchover of the drag coefficients, and an out-of-phase vortex shedding in general. As indicated by Fig. 8(c_3, d_3), the dominant frequency of the drag force is $f = 0.01$ while the vortex shedding frequency switches between $f = 0.11$ and $f = 0.16$. Furthermore, DMD modes at $f = 0.16$ and 0.11 are in AP and IP behaviours, respectively, see Fig. 9(*k*,*l*). This is consistent with the argument of Chen et al. (2020) and Yan et al. (2020, 2021) that the AP vortex shedding has a higher frequency than the IP one due to the confined space between the two gap vortices. Moreover, the appearance of the DMD mode at $f = 0.16$ indicates the development of the AP flow. As argued by Yan et al. (2020, 2021) the coexisting AP and IP modes of the vortex shedding are intrinsic to FF flows. Here, we suppose that the AP flow develops in a transient phase and interacts with the existing IP flow, which finally leads to the appearance of the FF-like flow. As shown in Fig. 9(*j*–*m*), the dominant DMD amplitude is possessed by a low-frequency mode at $f = 0.01$, and the corresponding vorticity contour is slightly biased due to the aperiodic fluctuation of the gap flow. Based on the frequency connection with the slowly fluctuating gap flow and its spatial distribution, we believe this mode is related to a pitchfork bifurcation (Mizushima and Ino, 2008), which finally leads to the symmetry-breaking of the wake. The pitchfork bifurcation is also found to be an intrinsic feature of FF flows in previous studies (Liu and Jaiman, 2016; Yan et al., 2020, 2021).

The main spectral components and flow fields in Phases IV (t^* = 550–700) and V (t^* > 700) are similar, to some extent, as depicted in Figs. 8(c_4,d_4,e_4) and 8(c_5,d_5,e_5). Correspondingly, as shown in Fig. 9(*n*–*u*), the spatial distribution of DMD modes in these two phases are approximately the same but with different compositions of initial amplitudes. Specifically, Phase IV is dominated by the gap-flow-related low-frequency mode (f = 0.01). For this mode, the gap flow is biased toward the lower cylinder, and vortices from the two cylinders have imbalanced strength, see Fig. 9(*q*). In Phase V, the low-frequency (f = 0.01) component in the drag spectrum is significantly damped, compared to that in Phase IV. Meanwhile, the mode that is related to the upper vortex street with f = 0.08 becomes dominant (b^* = 13%) and its harmonic modes (e.g., f = 0.16) are evenly allocated on the limit cycle, suggesting a periodic vortex shedding is formed in this phase. On the contrary, although with a frequency at f = 0.16, the third-dominant mode shown in Fig. 9(*o*) could result from the transient nature of Phase IV, rather than a harmonic mode with f = 0.08 in Fig. 9(*p*). Such a difference between the last two phases can be verified by the drag and lift coefficients of the two cylinders, which are out-of-phase at the beginning of Phase IV. This might help to explain the highly biased spatial distribution in the mode with f = 0.16. After roughly t^* = 650, the force coefficients of the two cylinders are overall in-phased, if the slight multi-frequency character of the lower cylinder is ignored, as shown in Fig. 9(*a,b*). The HHT results in Fig. 10 further confirm that the phase lag between the drag coefficients of the two cylinders fluctuates around 0 (0°) after t^* = 800, and the lift coefficients are roughly IP with a slight phase lag at 0.18π (32.9°). This explains the loosely IP distribution of the dominant upper vortex shedding mode at f = 0.08 in Phases IV and V.

Compared to the AAP flow, the typical DF flow is intrinsically dominated by the overall IP vortex shedding at the final stage, with only one cylinder's wake having a noticeable vortex shedding and the other one generally maintaining the IP synchronization with it. Similarly, the DF flow begins with a typical AP vortex shedding, but the IP mode at the beginning phase predominates in the following phases because of the unstable interactions between the two vortex streets. During the flow transition, a mode that acts like a shift mode may appear. When the asymmetry appears, a DMD mode that is related to a pitchfork bifurcation also appears with a frequency that matches the slow oscillation of the gap flow. At the final stage of the DF flow development, the wake becomes highly biased and one of the vortex streets is considerably weakened. Interestingly, in the dominant vortex shedding modes, the two vortex streets remain loosely the IP distributed, and this is further verified by the HHT result.

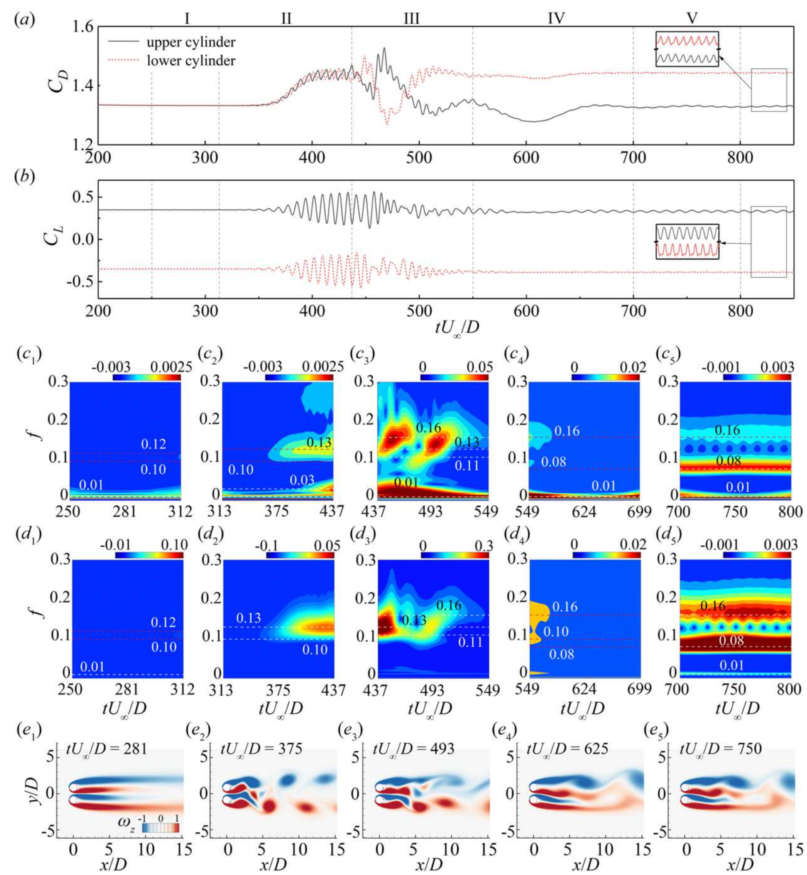

FIG. 8. Evolution of the tDF flow at s/D = 1.7 and Re = 80: (*a*,*b*) time histories of the drag and lift coefficients, (*c*,*d*) WT results of the drag and lift coefficients of the upper cylinder, and (*e*) *z*-vorticity contours. (c_1,d_1,e_1) for the initial phase at t^* = 250–313, (c_2,d_2,e_2) for the developing phase at t^* = 313–437, (c_3,d_3,e_3) for the transient phase at t^* = 437–550, (c_4,d_4,e_4) for the pre-stable phase at t^* = 550–700, (c_5,d_5,e_5) for the stable phase at t^* = 700–800. Here, I, II, III, IV, and V in (*a*) and (*b*) denote the initial, developing, transient, pre-stable, and stable phases, respectively.

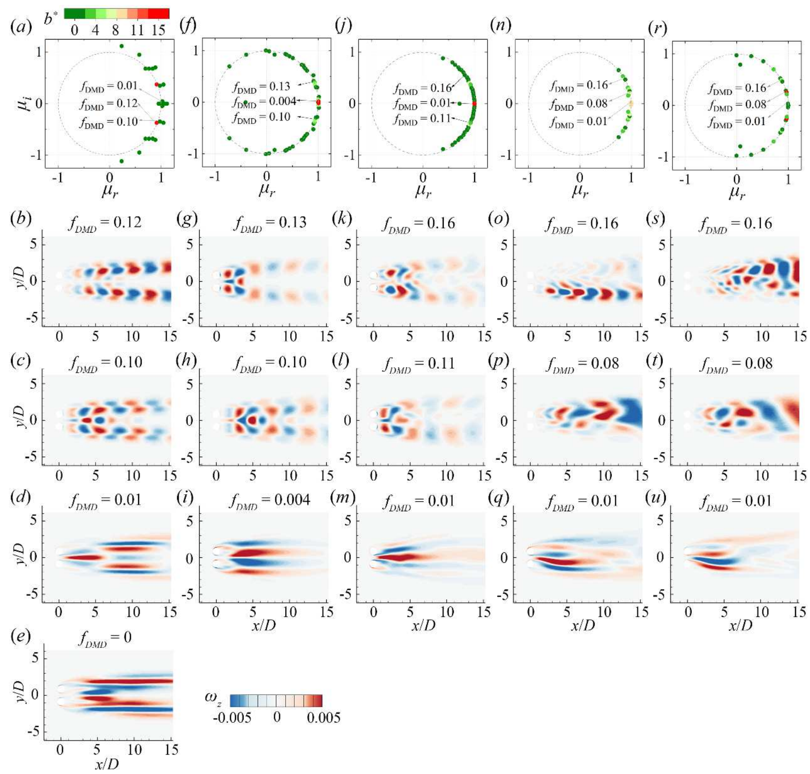

FIG. 9. DMD spectrum and modes with the most significant amplitude b^* at s/D = 1.7 and Re = 80: (*a*–*e*) for the initial phase at t^* = 250–313, (*f*–*i*) for the developing phase at t^* = 313–437, (*j*–*m*) for the transient phase at t^* = 437–550, (*n*–*q*) for the pre-stable phase at t^* = 550–700, and (*r*–*u*) for the stable phase at t^* = 700–800.

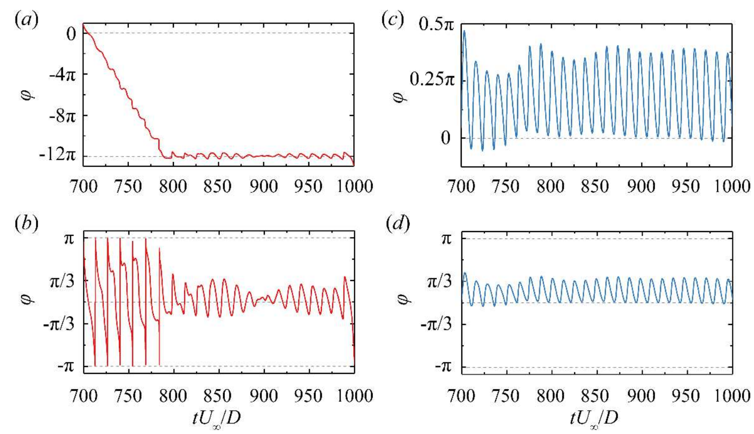

FIG. 10. Phase lag of the force coefficients between the upper and lower cylinders, calculated by HHT. (*a*,*b*) for the drag coefficients and (*c*,*d*) for the lift coefficients.

3.3.2 Evolution of special deflected flow

Figures 11 and 12 display the flow development and DMD results for the special DF (sDF) flow. At first glance, this evolution process is similar to that of the typical DF flow: i) in Phase I, the main DMD modes of vortex shedding are both in an overall IP manner; ii) the DMD mode of the gap flow in Phase III at $f = 0.01$ has a great similarity of the pitchfork bifurcation mode in the FF flow (Mizushima and Ino, 2008), matching well with the slowly swaying gap flow; iii) in Phases IV–V, DMD modes of the vortex shedding are highly asymmetric, related to the gap flow deflection. However, compared to the tDF flow, a noticeable low-frequency fluctuation is observed in the envelope of the lower cylinder drag coefficients, see Fig. 11(c_4, c_5), which is associated with a stronger gap flow oscillation. As a result, the phase lag in Fig. 13 is no longer stable like that of the tDF flow shown in Section 3.3.1. Instead, the drag force's phase lag grows from 0 (0°) to π (180°), then back and forth rapidly, which repeats roughly each period of the slow drag fluctuation of the lower cylinder. Meanwhile, although with constant accumulation, the lift force's phase lag fluctuates around 0 (0°), which explains the loosely IP DMD modes of the vortex shedding in the last two phases.

To further differentiate the two DF flows, we pay attention to the vortex dynamics in Phase V and investigate what causes the noticeable low-frequency oscillation in the sDF flow. As shown in Figs. 11(a,c_5) and 12(u), a low-frequency mode with $f = 0.01$, associated with the gap flow oscillation, is noticeable. Modulated by this low-frequency component, the drag coefficients of the two cylinders display an evident wave-like feature. It seems that the sDF flow has combined traits of tDF and FF flows. However, in contrast to the FF flow, the gap flow in the sDF flow is not strong enough to switch its deflection entirely from one side to the other, thus remaining deflected upward with apparent oscillations. As a result, the drag forces of the two cylinders display no switchover as those in the FF flow.

A major difference between the tDF and sDF flows is reflected by the HHT phase lag. In the tDF flow, the drag and lift phase lags between the two cylinders eventually become stable in the adjacent of 0°, while a noticeable phase lag accumulation and periodic variation appear in the sDF flow.

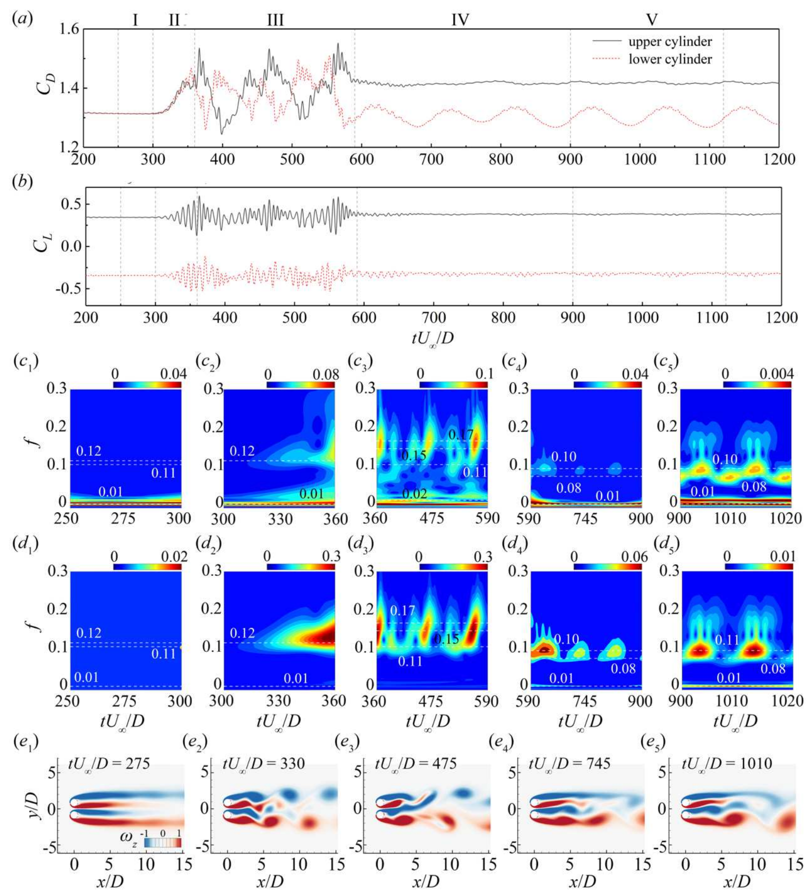

FIG. 11. Evolution of the special DF flow at s/D = 1.7 and Re = 84: (*a*,*b*) time histories of the drag and lift coefficients, (*c*,*d*) WT results of the drag and lift coefficients of the upper cylinder, and (*e*) *z*-vorticity

contours. (c_1,d_1,e_1) for the initial phase at t^* = 200–300, (c_2,d_2,e_2) for the developing phase at t^* = 300–360, (c_3,d_3,e_3) for the transient phase at t^* = 360–590, (c_4,d_4,e_4) for the pre-stable phase at t^* = 590–900, and (c_5,d_5,e_5) for the stable phase at t^* = 900–1200. Here, I, II, III, IV, and V in (*a*) and (*b*) denote the initial, developing, transient, pre-stable, and stable phases, respectively.

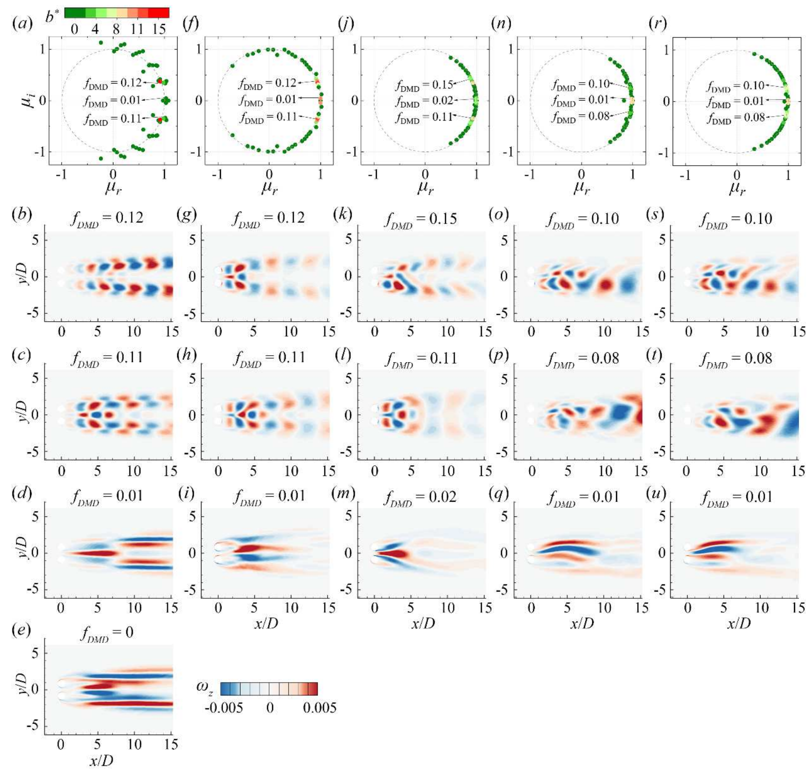

FIG. 12. DMD spectrum and modes with the most significant amplitude b^* at *s*/*D* = 1.7 and *Re* = 84: (*a*–*e*) for the initial phase at t^* = 200–300, (*f*–*i*) for the developing phase at t^* = 300–360, (*j*–*m*) for the transient phase at t^* = 360–590, (*o*–*q*) for the pre-stable phase at t^* = 590–900, and (*r*–*u*) for the stable phase at t^* = 900–1200.

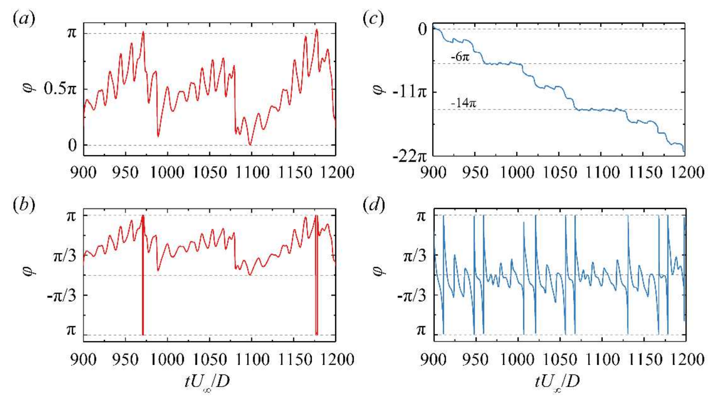

FIG. 13. Phase lag of the force coefficients between the upper and lower cylinders, calculated by HHT. (*a*,*b*) for the drag coefficients and (*c*,*d*) for the lift coefficients.

3.4 Evolution of in-phase flow

The IP flow, featured by the IP behaviour between the lift coefficients of the two cylinders, is a unique wake pattern in terms of asymmetry. As shown in Fig. 4, its flow field is asymmetric to the central line of the domain, although the two vortex streets are equally distributed with the same strength and breadth. From Fig. 3, the edge of the IP flow region tends to attenuate in a high-*Re* scenario ($Re > 175$), and this might indicate an incompatibility between the IP flow and the 3-D effect that arises around $Re \sim 180$ (Williamson, 1985). In this Section, we perform a 2-D simulation to generate an IP pattern at $s/D = 2.25$ and a supercritical *Re* of 186, examining the wake development using WT and DMD analyses. Then, we compare the 2-D simulation results with the 3-D ones under the same configuration, to obviate other possible factors, and to further scrutinize how the 3-D vortical structures interfere with the IP flow development.

3.4.1 Two-dimensional evolution of in-phase flow

As previously discussed, it is expected to find the typical AP flow feature in Phase I ($t^* < 1100$), see Fig. 14(*a*,*b*). Specifically, the drag coefficients of the two cylinders are overlapped while the lift coefficients are anti-phased. From Fig. 14(c_1,d_1) one can see that both drag and lift coefficients are dominated by the vortex shedding frequency $f = 0.22$, while WT results of drag coefficients also show the second harmonic frequency $f = 0.44$. However, in a single-cylinder case, the drag-to-lift frequency ratio is usually two. Compared to that, the dominant drag frequency in the side-by-side configuration is halved because of the asymmetric vortex shedding with respect to the central line of one cylinder due to the existence of the other cylinder (Chen et al., 2020, 2022). In terms of the vortex distribution, the wake in Fig. 14(e_1) appears to be similar to a typical AP flow. Correspondingly, the dominant DMD mode (b^* = 29%) at the vortex shedding frequency (f = 0.22) is also with two series of AP distributed vorticity, see Fig. 15(a,b). Nevertheless, as shown in Fig. 15(c), another mode is also detected under the same frequency but with a much smaller initial amplitude (b^* < 1%). With such a trivial amplitude, this mode with an IP vorticity distribution implies a further flow development similar to that at the beginning of the AAP and DF flows.

In Phase II (t^* = 1100–1210), the discrepancy of the drag coefficients of the two cylinders becomes perceivable at the end of this stage, see Fig. 14(a,b), which signifies a symmetry-breaking of the wake. Accordingly, the amplitude of the IP mode at f = 0.22 increases, see Fig. 15(e). In Phase III (t^* = 1210–1287), the wake asymmetry grows further, and the drag coefficients of the two cylinders display significant discrepancies. Besides, a low-frequency component with f = 0.01 appears, as shown in Figs. 14(c_3) and 15(l). Similar to the above-mentioned reason, this component is related to the nonlinear interactions between the AP mode at f = 0.22 (b^* ~ 14%) and the mode at f = 0.21 (b^* ~ 8%) that shows an asymmetric pattern, see Fig. 15(i–k). It is believed that this mode originates from the IP vorticity mode in Phase I.

In Phase IV (t^* = 1287–1350), the phase lag of lift coefficients approaches zero and the typical IP flow with a fluctuating frequency f = 0.20 dominates after $t^* \approx 1310$. Evidently, the AP mode is no longer found in this phase. However, the low-frequency component at f = 0.05, as shown in Fig. 14(c_4), suggests that the wake transition has not been completed yet. In Phase V (t^* > 1350), a clear IP behaviour is signified by the temporal variation of the lift coefficients. Owing to the strengthened second harmonic component f = 0.40, a significant peak is perceived in the time histories of drag coefficients. In this phase, the vortex shedding frequency is f = 0.20 without any perceivable low-frequency component, signifying a fully developed IP flow, see Fig. 14(d_4,d_5). As displayed in Fig. 14(e_4,e_5), each gap-side vortex of the two cylinders is separated into two comparable parts. One part is merged with the vortex shed from the freestream side of the neighbouring cylinder while the other part pairs with the vortex shed from the freestream side of the same cylinder, forming a wide 2P vortex-shedding pattern in the wake (Williamson, 1985; Chen et al., 2020). Comparing the IP mode in successive phases, the strength of this mode increases while the frequency decreases, see Fig. 15(n,r). The asymmetric mode in Phase III has an intermediate amplitude and frequency. Moreover, the IP modes before and after the wake transition are different from each other, indicated by the distinct *z*-vorticity contours and unequal modal frequencies.

Compared to the DF flow, the IP vortex shedding fully predominates after the flow becomes stable in the IP flow. Specifically, similar to other flow patterns, the development of IP flow in the 2-D scenario also begins with an AP vortex shedding, with a DMD mode of the IP vorticity distribution appearing next to the dominant AP mode on the spectrum but having a trivial amplitude. Owing to the dissipating AP vortex shedding, the initial amplitude of this IP mode gradually increases from below 1% to over 40%, eventually solely predominating, and the two vortex streets also become strictly IP. This process is in line with the IP flow in the 2-D scenario reported by Yan et al. (2021). However, as shown in the following section, this IP mode is not detected in the 3-D simulation, which eventually becomes the AP flow.

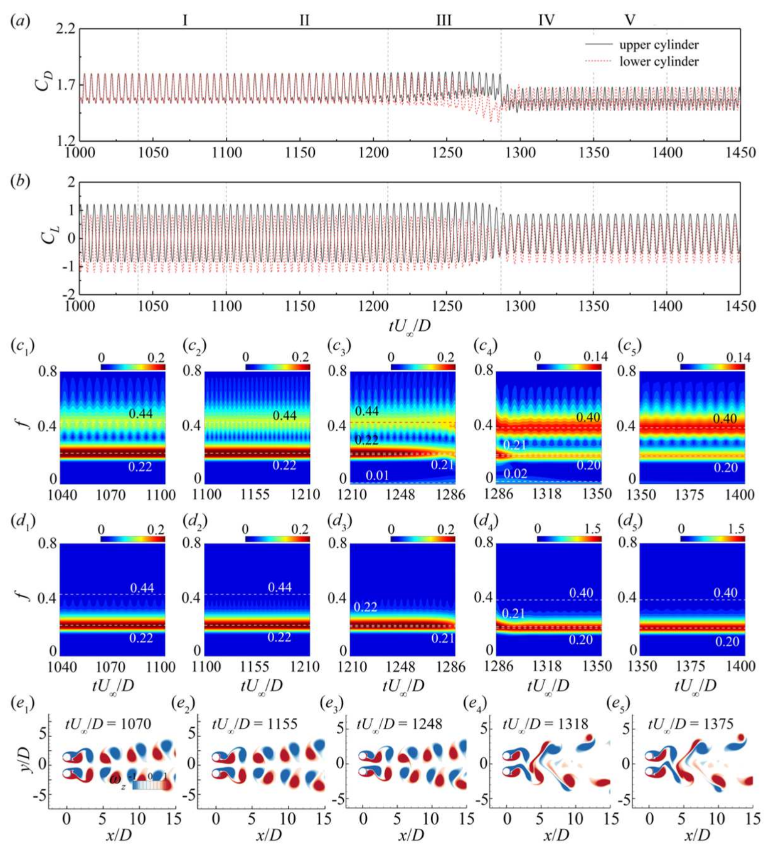

FIG. 14. Evolution of the IP flow at s/D = 2.25 and Re = 186 using 2-D simulation: (*a*,*b*) time histories of the drag and lift coefficients, (*c*,*d*) WT results of the drag and lift coefficients of the upper cylinder, and (*e*) vorticity contours. (c_1,d_1,e_1) for the initial phase at t^* = 1040–1100, (c_2,d_2,e_2) for the developing phase at t^* = 1100–1210, (c_3,d_3,e_3) for the transient phase at t^* = 1210–1287, (c_4,d_4,e_4) for the pre-stable phase at t^* = 1287–1350, and (c_5,d_5,e_5) for the stable phase at t^* = 1350–1400. Here, I, II, III, IV, and V in (*a*) and (*b*) denote the initial, developing, transient, pre-stable, and stable phases, respectively.

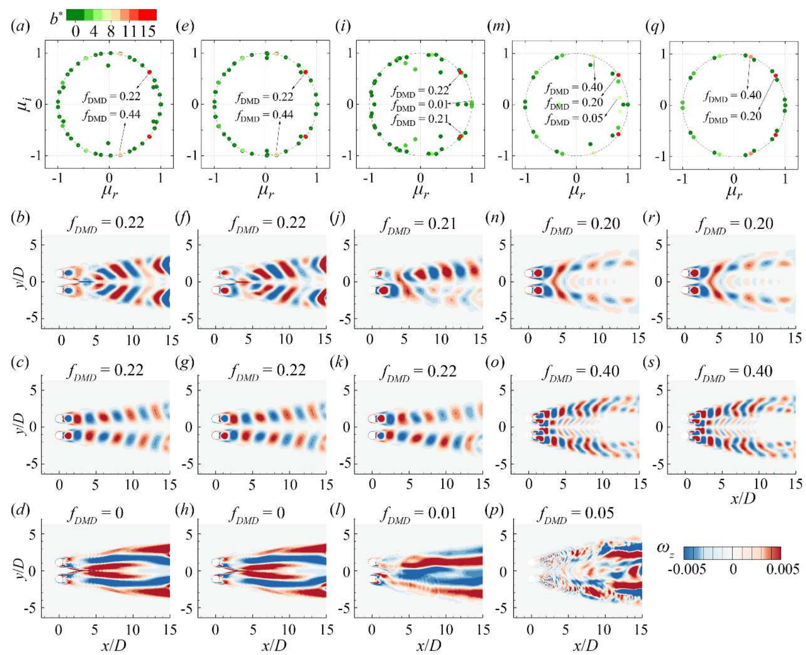

FIG. 15. DMD spectrum and modes with the most significant amplitude b^* at s/D = 2.25 and Re = 186 using 2-D simulation: (*a*–*d*) for the initial phase at t^* = 1040–1100, (*e*–*h*) for the developing phase at t^* = 1100–1210, (*i*–*l*) for the transient phase at t^* = 1210–1287, (*m*–*p*) for the pre-stable phase at t^* = 1287–1350, and (*q*–*s*) for the stable phase at t^* = 1350–1400.

3.4.2 Evolution of the wake in the 3-D case

In this section, we aim to reveal the influences of 3-D vortical structures on wake development by analysing the 3-D DNS with the same parameters as in Section 3.4.1. To ensure comparability, the computational grid employed in this 3-D case is an extension of the 2-D mesh in Section 2.1. In other words, the x-y projection of this grid is exactly the same as that shown in Fig. 1, with the surface extended

10D in the z-direction, see Fig. 16 (only the outline of the upper and lower surfaces, and the cylinder are shown for better visuality). The upper and lower surfaces of the domain are given as periodic boundaries, and the left and right surfaces are inflow and outflow boundaries, respectively. The rest of the boundary conditions are the same as those in the 2-D mesh shown in Section 2.1. Compared to the previous literature (Kang 2003), the difference of this grid calculated was within 3% ($C_{D,mean}$ = 1.476, S_t = 0.159 at s/D = 2.5, Re = 100). Complete convergence and robustness tests have been reported in Yan et al. (2020).

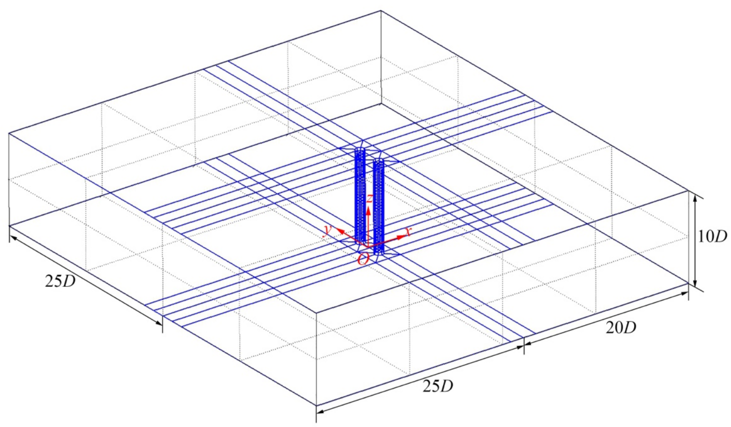

FIG. 16. Computational domain for the 3-D DNS case.

As shown in Fig. 17(a,b), in the 3-D case, force coefficients together with the vortex shedding of the two cylinders remain AP throughout the flow development. The expected IP flow does not occur, thus indicating a distinct process from that in the 2-D case. In Phases I (t^* = 56–146) and II (t^* = 146–236), the drag coefficients of the two cylinders are overlapped and the lift coefficients are perfectly anti-phased, signifying a clear AP flow character. The 3-D flow fields shown in Fig. 17(e_1,f_1,e_2,f_2) further verify the AP vortex shedding. In the spanwise direction, these vortex tubes are synchronized and uniform, showing no hints of a formation of the streamwise vortices. Correspondingly, the dominant 3-D DMD mode at f = 0.22 (b^* = 37% and b^* = 14% for Phases I and II, respectively) matches well with this trend, where no streamwise vorticity is detected, see Fig. 18(b_1,b_2). Noticeably, two very similar modes are non-harmonic of the dominant mode appearing in these two phases. These modes are adjacent to the dominant mode in the spectrum, although with only a trivial initial amplitude (b^* < 0.1%). Unlike the 2-D case, these two modes have no connection with the IP vorticity. Instead, their spatial distributions concentrate on the far-wake region, and the latter one in the developing phase seems to be closer to the upstream region, see Fig. 18(c_1,c_2).

In Phase III (t^* = 660–750), the drag coefficients of the two cylinders decrease slightly and so as the fluctuations of lift coefficients. However, the lift coefficients of the two cylinders are still anti-phased, evidenced by the vorticity contours shown in Fig. 17(e_3,f_3) and the dominant DMD mode at the vortex shedding frequency shown in Fig. 18(b_3). Evidently, the AP wake is not 'replaced' by the IP vortex shedding like in the 2-D case. As shown in Fig. 17(e_3), the streamwise vortical structures appear in the wake after about 2 shedding periods of the vortex tubes. In the development of streamwise vortices, the energy of spanwise vortices is extracted by the streamwise vortices. Correspondingly, the strength of spanwise vortices decreases significantly (Mansy et al., 1996; Papaioannou et al., 2006). Since the forces on the cylinders only come from the spanwise vortices, it is expected to see the decreased drag and lift coefficients. In other words, the wake transition, featured by the decreasing force coefficients, is closely associated with the appearance of streamwise vortices. Meanwhile, the mode shown in Fig. 18(c_3) appears next to the dominant mode on the spectrum, and its spatial distribution has better strength in the far-wake region. If compared to the similar modes shown in the last phases, this mode has vorticity that is closer to the upstream region and a slightly larger initial amplitude (b^* ~ 1%).

In Phases IV (t^* = 750–800) and V (t^* = 800–850), drag and lift coefficients fluctuate at a smaller frequency (f = 0.21) compared to those in the previous phases. As shown in Fig. 17(a,b), the overlapped drag coefficients and AP lift coefficients of the two cylinders unambiguously signify the persistence of the AP flow. Furthermore, as displayed in Fig. 17(d_4,d_5,e_4,e_5), streamwise vortices are still apparent in the wake and the vortex street can maintain the AP shape in a longer downstream distance, acting as a typical feature of AP flow (Williamson, 1985). Interestingly, the modes that have stronger vorticity in the far-wake region are not found in these two phases. As shown in Fig. 18(a_4,a_5), the only mode that appears next to the dominant mode (not shown here) is almost identical to the dominant mode itself, and other modes with noticeable initial amplitudes are harmonic to the dominant AP mode.

From the above analysis, we realize how 2-D and 3-D cases reveal completely different features. This major difference between 2-D and 3-D simulations under the same geometric configuration implies an incompatibility of the IP flow and the 3-D effect. The DMD results prove that the IP flow, or at least the IP vorticity mode, is incompatible with the 3-D scenario. This in a way explains the absence of IP flow in the 3-D case reported by Chen et al. (2022). Opposite to the IP mode that grows from a trivial initial amplitude and eventually predominates in the 2-D case, there is no IP mode from the beginning of the flow development in the 3-D case. Instead, only DMD modes that concentrate on the far wake region appear adjacent to the dominant AP mode. These modes are all located inside the unit cycle and dissipate after the wake transition, when the 3-D effect, i.e., the streamwise vortices, start to emerge. We may infer that these 3-D vortical structures disturb the development of IP mode, which finally leads to the incompatibility of the IP mode and the 3-D effects. Therefore, the IP flow does not exist in the 3-D configuration.

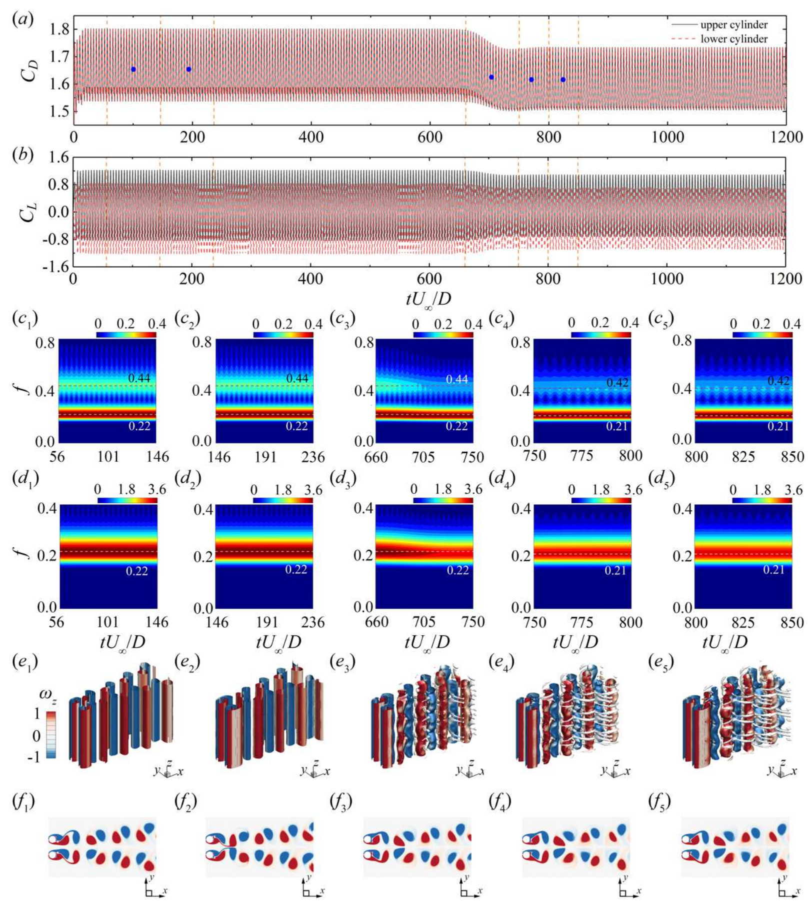

FIG. 17. Evolution of the wake at s/D = 2.25 and Re = 186 using 3-D simulation: (a,b) time histories of

the drag and lift coefficients, (*c*,*d*) WT results of the drag and lift coefficients of the upper cylinder, (*e*) 3-D vorticity fields, and (*f*) the corresponding slices extracted at z/D = 5.0. (e_1,f_1) for the initial phase at t^* = 102, (e_2,f_2) for the developing phase at t^* = 192, (e_3,f_3) for the transient phase at t^* = 705, (e_4,f_4) for the pre-stable phase at t^* = 777, and (e_5,f_5) for the stable phase at t^* = 828.

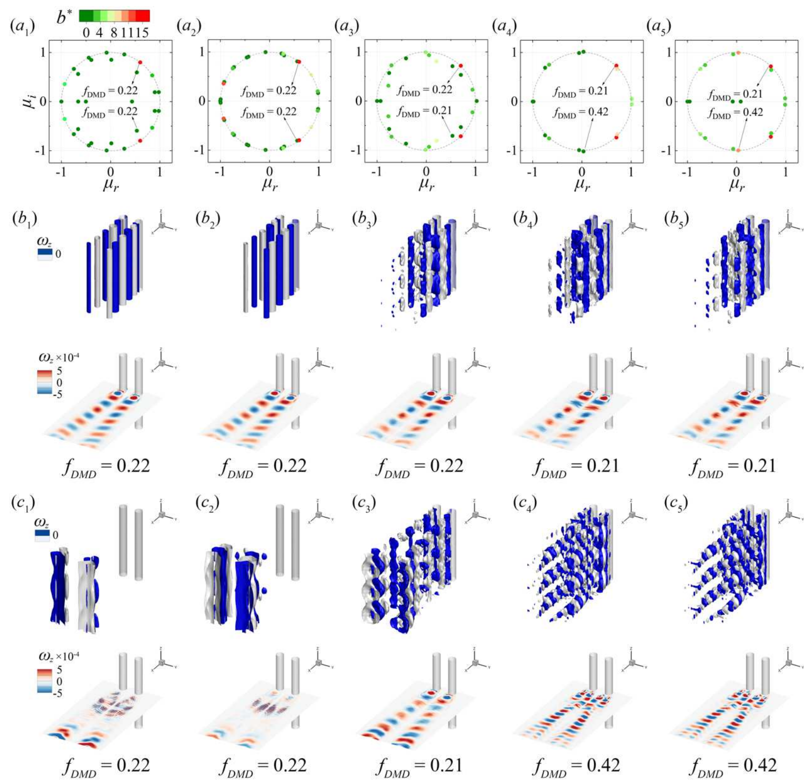

FIG. 18. DMD spectrum, iso-surface at $\omega_z = \mp 2.5\times10^{-4}$, and slice extracted at z/D = 7.5 for the case at s/D = 2.25 and Re = 186: (a_1,b_1,c_1) for period 1, (a_2,b_2,c_2) for period 2, (a_3,b_3,c_3) for period 3, (a_4,b_4,c_4) for period 4, and (a_5,b_5,c_5) for period 5.

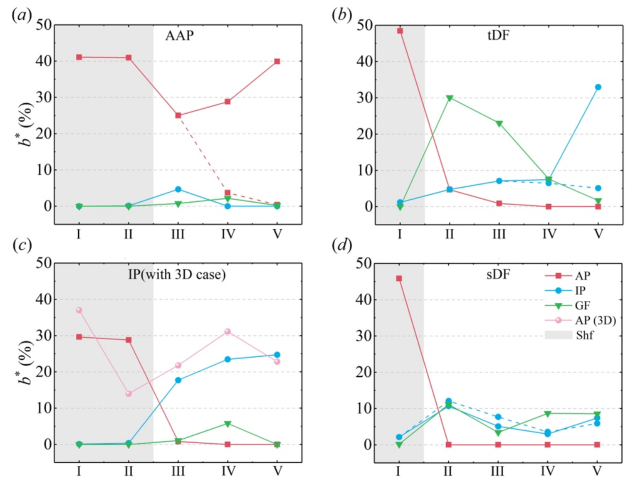

FIG. 19. Statistics of the initial amplitude of representative DMD modes: AP (anti-phase vortex shedding related), IP (in-phase vortex shedding related), GF (gap flow related), and Shf (shift mode related) for (*a*) s/D = 2.3 and Re = 50; (*b*) s/D = 1.7 and Re = 80; (*c*) s/D = 2.25 and Re = 186 (both 2-D and 3-D); (*d*) s/D = 1.7 and Re = 84.. The dashed line means that the two vortex streets become highly biased.

4. Concluding remarks

In this paper, we gained deep insights into the development of asymmetric wake patterns arising from the uniform flow past two parallel circular cylinders by using wavelet analysis of the forces, Hilbert-Huang transform of the phase lags, and dynamics mode decomposition of flow fields. We started with the wake map behind two side-by-side circular cylinders and then focused on wake patterns with asymmetry. In particular, the asymmetric anti-phase (AAP) and special deflected (sDF) flows that are newly discovered by the newly refined map, together with typical deflected (tDF) and in-phase (IP) flows. These four flow patterns are analytically investigated with the following principal findings.

1) During flow development, all flow patterns are determined by more than one single dynamic. Figure 19 summarizes the change of the initial amplitude of DMD modes representing different dynamics across five phases, including AP (anti-phase vortex pairs), IP (in-phase vortex pairs), GF (gap flow related), and Shf (shift mode related). The variation of these modes, especially AP and IP modes, helps to differentiate these flow patterns.
2) The AAP flow is featured by the narrow-wide vortex shedding while the two asymmetric, yet independent, vortex streets are anti-phased. In addition to the dominant AP mode, there is also

an IP mode that appears when the flow begins to show asymmetry and then dissipates when the asymmetric flow becomes stable. In general, the AAP flow is dominated by the AP mode but slightly influenced by the IP mode.

3) The tDF flow and sDF flow are featured by the biased IP vortex shedding, with only one cylinder's wake having a noticeable vortex shedding and the other one generally keeps in-phase behaviour with it. Although the DF flows are dominated by AP mode at first, the IP mode rapidly grows. When the amplitude of AP and IP modes are comparable, the flow becomes FF-like. Eventually, the AP mode dissipated and the IP mode took dominance. These two DF flows have different phase lags between two vortex streets in a fully developed flow.
4) The IP flow is featured by the spacially asymmetrical but temporally symmetric flow field, i.e., IP vortex shedding. In short, the AP mode at the beginning dissipates gradually and the IP mode grows rapidly, overtaking the dominance. This typical IP flow development is incompatible with the 3-D effect as a result of the disturbance of 3-D vortical structures in the development of IP mode.

This paper provides a comprehensive study of the possible dynamics that appeared in the flow development of four distinct flow patterns, which serves for future investigation such as machine learning in fluid mechanics and reduced order modelling of complex flows (Hou et al. 2022, Farzamnik et al. 2023, Wang et al. 2023). In addition, these findings are crucial to further understand asymmetric flow patterns arising from complete symmetric settings, which is deeply related to bifurcation flow, turbulent transitions, and nonlinear dynamic systems.

Acknowledgments. The work was carried out at the National Supercomputer Center in Tianjin, and the calculations were performed in the Tianhe 3 prototype.

Funding. This work was financially supported by the National Natural Science Foundation of China (Grants No. 51779172).

Declaration of interests. The authors report no conflict of interest.

Authors' contributions. Y. Y. and W. C. contributed equally to this paper as co-first authors.

Data Availability Statement. The data that support the findings of this study are available from the corresponding author upon reasonable request.

REFERENCES

Afgan, I., Kahil, Y., Benhamadouche, S. and Sagaut, P. "Large eddy simulation of the flow around single and two side-by-side cylinders at subcritical Reynolds numbers," *Phys. Fluids* **23**, 075101 (2011).

Alam, M. M., Moriya, M. and Sakamoto, H. "Aerodynamic characteristics of two side-by-side circular cylinders and application of wavelet analysis on the switching phenomenon," *J. Fluids Struct.* **18**, 325–346 (2003).

Alam, M. M. and Zhou, Y. "Flow around two side-by-side closely spaced circular cylinders," *J. Fluids Struct.* **23**, 799–805 (2007).

Bai, X.-D., Zhang, W. and Wang Y. "Deflected oscillatory wake pattern behind two side-by-side circular cylinders", *Ocean Eng.* **197**, 106847 (2020).

Barkley, D. "Linear analysis of the cylinder wake mean flow," *Europhys. Lett.* **75**(5), 750–756 (2006).

Bearman, P. W. and Wadcock, A. J. "The interaction between a pair of circular cylinders normal to a stream," *J. Fluid Mech.* **61**, 499–511 (1973).

Brun, C., Tenchine, D. and Hopfinger, E. J. "Role of the shear layer instability in the near wake behavior of two side-by-side circular cylinders," *Exp. Fluids* **36**, 334–343 (2004).

Carini, M., Giannetti, F. and Auteri, F. "On the origin of the flip-flop instability of two side-by-side cylinder wakes," *J. Fluid Mech.* **742**, 552–576 (2014).

Carini, M., Auteri, F. and Giannetti, F. "Secondary instabilities of the in-phase synchronized wakes past two circular cylinders in side-by-side arrangement," *J. Fluids Struct.* **53**, 70–83 (2015).

Cantwell, C. D., Moxey, D., Comerford, A., Bolis, A., Rocco, G., Mengaldo, G., De Grazia, D., Yakovlev, S., Lombard, J. E., Ekelschot, D., Jordi, B., Xu, H., Mohamied, Y., Eskilsson, C., Nelson, B., Vos, P., Biotto, C., Kirby, R. M. and Sherwin, S. J. "Nektar++: Am open-source spectral/hp element framework," *Comput. Phys. Communication.* **192**, 205-219 (2015).

Chen, W., Ji, C., Alam, M. M., Williams, J. and Xu, D. "Numerical simulations of flow past three circular cylinders in equilateral-triangular arrangements," *J. Fluid Mech.* **891**, A14 (2020).

Chen, W., Ji, C., Xu, W., Liu, S. and Campbell, J. "Response and wake patterns of two side-by-side elastically supported circular cylinders in uniform laminar cross-flow," *J. Fluids Struct.* **55**, 218–236 (2015).

Chen, W., Ji, C., Alam, M. M. and Yan, Y. "Three-dimensional flow past two stationary side-by-side circular cylinders," *Ocean Eng.* **244**, 110379 (2022).

Chen, W., Yan, Y., Ji, C., Alam, M. M., Srinil, N., Noack, B. R., and Deng, N. "Revisit the intrinsic features of flip-flopping flow behind side-by-side circular cylinders," *J. Fluid Mech.* (2023), (Under review).

Deng, N., Noack, B. R., Morzyski, M. and Pastur, L. R. "Low-order model for successive bifurcations of the fluidic pinball," *J. Fluid Mech.* **884**, A37 (2020).

Farge, M. "Wavelet transforms and their applications to turbulence," *Annu. Rev. Fluid Mech.* **24**, 395–457 (1992).

Farzamnik, E., Ianiro, A., Discetti, S., Deng, N., Oberleithner, K., Noack, B. and Guerrero, V. "From snapshots to manifolds – a tale of shear flows," *J. Fluid Mech*. **955**, A34 (2023).

Giannetti, F. and Luchini, P. "Structural sensitivity of the first instability of the cylinder wake," *J. Fluid Mech.* **581**, 167–197 (2007).

Guermond, J. L. and Shen, J. "Velocity-correction projection methods for incompressible flows," *SIAM J. Numerical Analysis* **41**, 112-134 (2003).

Heil, M., Rosso, J., Hazel, A. L. and Brøns, M. "Topological fluid mechanics of the formation of the Kármán-vortex street," *J. Fluid Mech.* **812**, 199–221 (2017).

Ho, C. M. and Huerre, P. "Perturbed free shear layers," *Annu. Rev. Fluid Mech.* **16**, 365–424 (1984).

Hou, C., Deng, N., and Noack, B. R. "Trajectory-optimized cluster-based network model for the sphere wake," *Phys. Fluids* **34**, 085110 (2022).

Huang, N. E. and Shen, S. S. P. "Hilbert–Huang Transform and Its Applications," 2nd ed. Vol. 16. Interdisciplinary Mathematical Sciences. New Jersey: World Scientific (2014).

Huang, N. E., Wu, Z., Long, S. R.,Arnold, K. C., Chen, X. and Blank, K. "On Instantaneous Frequency," *Advances in Adaptive Data Analysis* **1**(2), 177–229 (2009).

Huerre, P. and Monkewitz, P. A. "Local and Global Instabilities in Spatially Developing Flows," *Annu. Rev. Fluid Mech.* **22**, 473–537 (1990).

Jiang, H., Cheng, L., Draper, S., An, H. and Tong, F. "Three-dimensional direct numerical simulation of wake transitions of a circular cylinder," *J. Fluid Mech.* **801**, 353–391 (2016).

Jovanovic, M. R., Schmid, P. J. and Nichols, J. W. "Sparsity-promoting dynamic mode decomposition," *Phys. Fluids* **26**(2), 024103 (2014).

Karniadakis, G. E., Israeli, M. and Orszag, S. A. "High-order splitting methods for the incompressible Navier-Stokes equations," *J. Comput. Phys*. **97**, 414-443 (1991).

Karniadakis, G. E. and Sherwin, S. J. "Spectral/hp element methods for computational fluid dynamics," 2nd ed. Oxford University Press, Oxford, UK (2005).

Kang, S. "Characteristics of flow over two circular cylinders in a side-by-side arrangement at low Reynolds numbers," *Phys. Fluids* **15**, 2486–2498 (2003).

Kim, H. J. and Durbin, P. A. "Investigation of the flow between a pair of circular cylinders in the flopping regime," *J. Fluid Mech.* **196**, 431–448 (1988).

Kutz, J. N., Brunton, S. L., Brunton, B. W. and Proctor, J. L. "Dynamic Mode Decomposition: Data-Driven Modeling of Complex Systems," *SIAM* (2016).

Liu, B. and Jaiman, R. K. "Interaction dynamics of gap flow with vortex-induced vibration in side-by-side cylinder arrangement," *Phys. Fluids* **28**, 127103 (2016).

Liu, K., Ma, D.-J., Sun, D.-J. and Yin, X.-Y. "Wake patterns of flow past a pair of circular cylinders in side-by-side arrangements at low Reynolds numbers," *J. Hydrodyn.* Ser. B **19**(6), 690−697 (2007).

Marquet, O., Sipp, D. and Jacquin, L. "Sensitivity analysis and passive control of cylinder flow," *J. Fluid Mech.* **615**, 221–252 (2008).

Mansy, H., Yang, P.-M., and Williams, D. R. "Quantitative measurements of three-dimensional structures in the wake of a circular cylinder," *J. Fluid Mech*. **270**, 271–296 (1994).

Meneghini, J. R., Satara, F., Siqueira, C. L. R. and Ferrari, J. A. "Numerical simulation of flow interference between two circular cylinders in tandem and side-by-side arrangements," *J. Fluids Struct.* **15**, 327–350 (2001).

Mizushima, J. and Ino, Y. "Stability of flows past a pair of circular cylinders in a side-by-side arrangement," *J. Fluid Mech.* **595**, 491-507 (2008).

Mondal, R. and Alam, M. M., "Blockage effect on wakes of various bluff bodies: A review of confined flow," *Ocean Eng.* **286**, 115592 (2023).

Moxey, D., Cantwell, C. D., Yan, B., Cassinelli, A., Castiglioni, G., Chun, S., Juda, E., Kazemi, E., Lackhove, K., Marcon, J., Mengaldo, G., Serson D., Turner, M., Xu, H., Peiro, J., Kirby, R. M. and Sherwin, S. J. "Nekter++: Enhancing the capability and application of high-fidelity spectral/hp element methods," *Comput. Phys. Communications* **249**, 107110 (2020).

Muhammad, Z., Alam, M. M., Ji, C., Zhu, H., and Noack, B. R. "Asymmetric wake, origin, generation, and suppression behind asymmetrically pitching hydrofoil," *Ocean Eng.* **266**, 112466 (2022).

Noack, B. R., Afanasiev, K., Morzyński, M., Tadmor, G. and Thiele, F. "A hierarchy of low-dimensional models for the transient and post-transient cylinder wake," *J. Fluid Mech.* **497**, 335–363 (2003).

Noack, B. R., Stankiewicz, W., Morzyński, M. and Schmid, P. J. "Recursive dynamic mode decomposition of transient and post-transient wake flows," *J. Fluid Mech.* **809**, 843-872 (2016).

Park, D. and Yang, K.-S. "Flow instabilities in the wake of a rounded square cylinder," *J. Fluid Mech.* **793**, 915–932 (2016).

Papaioannou, G. V., Yue, D. K. P., Triantafyllou, M. S. and Karniadakis, G. E. "Three-dimensionality effects in flow around two tandem cylinders," *J. Fluid Mech.* **558**, 387–413 (2006).

Pang, J. H., Zong, Z., Zou, L. and Wang., Z. "Numerical simulation of the flow around two side-by-side circular cylinders by IVCBC vortex method," *Ocean Eng.* **119**, 86–100 (2016).

Peschard, I. and Le Gal, P. "Coupled wakes of cylinders," *Phys. Rev. Lett.* **77**, 3122–3125 (1996).

Qi, X., Dai, S., Ren, C., Dong, Q., and Xiong, C., "Numerical simulation of flow-induced vibration of a circular cylinder close to a free surface at low Reynolds number," Phys. Fluids **35**, 043108 (2023).

Ren, C., Cheng, L., Xiong, C., Tong, F. and Chen, T. "Bistabilities in two parallel Kármán wakes," *J. Fluid Mech.* **929**, A5 (2021).

Roshko, A. "On the drag and shedding frequency of two-dimensional bluff bodies," *NACA Tech. Rep.*1191 (1954).

Rowley, C. W., Mezic, I., Bagheri, S., Schlatter, P. and Henningson, D. S. "Spectral analysis of nonlinear flows," *J. Fluid Mech.* **641**, 115–127 (2009).

Schmid, P. J. "Dynamic mode decomposition of numerical and experimental data," *J. Fluid Mech.* **656**, 5–28 (2010).

Shao, J. and Zhang, C. "Large eddy simulations of the flow past two side-by-side circular cylinders," *Intl J. Comput. Fluid Dyn.* **22** (6), 393–404 (2008).

Singha, S., Nagarajan, K. K. and Sinhamahapatra, K. P. "Numerical study of two-dimensional flow around two side-by-side circular cylinders at low Reynolds numbers," *Phys. Fluids* **28**, 053603 (2016).

Sumner, D., Wong, S. S. T., Price, S. J. and Païdoussis, M. P. "Fluid behavior of side-by-side circular cylinders in steady cross-flow," *J. Fluids Struct.* **13**, 309–339 (1999).

Sumner, D. "Two circular cylinders in cross-flow: A review," *J. Fluids Struct.***26**, 849–899 (2010).

Supradeepan, K. and Roy, A. "Characterisation and analysis of flow over two side by side cylinders for different gaps at low Reynolds number: A numerical approach," *Phys. Fluids* **26**, 063602 (2014).

Thapa, J., Zhao, M., Cheng, L. and Zhou, T. M. "Three-dimensional simulations of flow past two circular cylinders in side-by-side arrangements at right and oblique attacks," *J. Fluids Struct.* **55**, 64–83 (2015).

Tong, F. F., Cheng, L. and Zhao, M. "Numerical simulations of steady flow past two cylinders in staggered arrangements," *J. Fluid Mech.* **765**, 114–149 (2015).

Turton, S. E., Tuckerman, L. S. and Barkley, D. "Prediction of frequencies in thermosolutal convection from mean flows," *Phys. Rev. E* **91**(4), 043009 (2015).

Ullah, N. and Zhou, C.Y. "Fluid dynamics of flow around side-by-side arranged cylinders", *Arabian J. Sci. Eng.* **45** (7), 5907–5923 (2020).

Wang, X., Deng, N., Cornejo Maceda, G. Y., and Noack, B. R., "Cluster-based control for net drag reduction of the fluidic pinball," *Phys. Fluids* **35**, 023601 (2023)

Wang, Z. J., Zhou, Y. and Li, H. "Flow-visualization of a two side-by-side cylinder wake," *J. Flow Visual. Image Process.* **9**, 123–138 (2002).

Wang, Z. J. and Zhou, Y. "Vortex interactions in a two side-by-side cylinder near-wake," *Int. J. Heat Fluid Flow*. **26**, 362–377 (2005).

Williamson, C. H. K. "Evolution of a single wake behind a pair of bluff bodies," *J. Fluid Mech.* **159**, 1–18 (1985).

Wu, G., Lin, W., Du, X., Shi C. and Zhu, J. "On the flip-flopping phenomenon of two side-by-side circular cylinders at a high subcritical Reynolds number of $1.4\ 10^{5}$", *Phys. Fluids* **32**, 094112 (2020).

Xu, H., Cantwell, C. D., Monteserin, C., Eskilsson, C., Engsig-Karup, A. P. and Sherwin, S. J. "Spectral/hp element methods: Recent developments, applications, and perspectives," *J. Hydrodyn*. **30**, 1–22 (2018).

Xu, S. J., Zhou, Y. and So, R. M. C. "Reynolds number effects on the flow structure behind two side-by-side cylinders," *Phys. Fluids* **15**, 1214–1219 (2003).

Yan, Y., Ji, C. and Srinil, N. "Three-dimensional flip-flopping flow around a pair of dual-stepped circular cylinders in a side-by-side arrangement," *Phys. Fluids* **32**(12), 123608 (2020).

Yan, Y., Ji, C. and Srinil, N. "On wake modulation and interaction features of a pair of dual-step circular cylinders in side-by-side arrangements," *Phys. Fluids* **33**(9), 093604 (2021).

Zdravkovich, M. M. "Review of flow interference between two circular cylinders in various arrangements," *Trans. ASME: J. Fluids Engng* **99**, 618–633 (1977).

Zdravkovich, M. M.. "Flow Around Circular Cylinders*,* vol 1: Fundamentals," Oxford University Press, UK (1997).

Zeng, C., Qiu, F., Zhou, J., Hu, Y. and Wang, L. "Large eddy simulation of flow around two side-by-side circular cylinders at Reynolds number 3900", *Phys. Fluids* **35**, 035102 (2023).

Zhao, M., Cheng, L. and An, H. "Numerical investigation of vortex-induced vibration of a circular cylinder in transverse direction in oscillatory flow," *Ocean Eng.* **41**, 39–52 (2012).

Zhou, Y. and Alam, M. M. "Wake of two interacting circular cylinders: A review," *Int. J. Heat Fluid Flow* **62**, 510–537 (2016).

Zhou, Y., Zhang, H. J. and Yiu, M. W. "The turbulent wake of two side-by-side circular cylinders," *J. Fluid Mech.* **458**, 303–332 (2002).

Zhou, Y., Wang, Z. J., So, R. M. C., Xu, S. J. and Jin, W. "Free vibrations of two side-by-side cylinders in a cross flow," *J. Fluid Mech.* **443**, 197–229 (2001).